Investigation on p-type ZnO nanoparticles and their application to visible LEDs

RAJ DEEP
Fujita-Yoshida Laboratory

Submitted in partial fulfillment of the requirements for the degree of Doctor of Engineering at Shimane University.

Supervisor:
Prof. Dr. Yasuhisa Fujita
&
Assistant supervisor:
Prof. Dr. Yasuji Yamada
Prof. Dr. Hiroji Masuda
Assoc. Prof. Dr. Toshiyuki Yoshida

Graduate School of Natural Science and Technology

Shimane University, Japan

August 2024

Table of contents

Table of Figures

Lists of Tables

Abstract

In this study, p-type ZnO nanoparticles (NPs) were synthesized by the arc-discharge method, and utilizing these NPs, homojunction light-emitting diodes (LEDs) were fabricated and studied. The fabrication of ZnO NPs was monitored and studied in situ by controlling the plasma parameters. The dependence of ZnO NPs nitrogen concentration on the performance of ZnO nanoparticle-based LEDs has been explained through optical emission spectroscopy techniques. Nitrogen dopants in ZnO NPs can become acceptors, more advantageously at lower plasma temperatures during the manufacturing process. The nanocrystals ZnO have been characterized for structure using X-ray diffraction and scanning electron microscopy, and optically by Raman spectroscopy and photoluminescence spectroscopy.

The role of defects in the acceptor properties of NPs was studied by annealing ZnO NPs in oxygen and nitrogen environments. Annealing of nitrogen-doped ZnO NPs in a nitrogen environment was shown to increase the number of zinc vacancies. Conversely, annealing in an oxygen environment results in a higher number of oxygen vacancies due to the desorption of nitrogen. The contribution of zinc vacancies to acceptor formation in nitrogen-doped ZnO NPs, as studied by photoluminescence, was confirmed for the first time by actual device formation. The primary factor contributing to the p-type behavior is the synergistic influence of acceptor doping and zinc deficiency in nitrogen-doped ZnO NPs.

The thermal impact of LEDs was studied on aluminum-based LEDs by current injection and by thermoelectric methods. The ultraviolet (UV) intensity exhibits an initial increase as the injection current rises towards the saturation limit, accompanied by a shift in the peak position. Subsequently, at higher injection currents and at higher temperatures, the UV intensity decreases. The UV light emitted by the ZnO-based LEDs was down-converted into visible light by utilizing phosphors.

Optically stable and high-color rendering index white light was fabricated using a multi-phosphor-based approach.

Keywords: p-type ZnO, ZnO homojunction LED, annealing atmosphere, nitrogen doping, phosphor-converted LEDs, UV electroluminescence.

Introduction

The progress in electronic and optoelectronic devices is frequently driven by the creation of novel material systems that possess superior properties compared to existing materials. In the electronics industry, there was a shift from using germanium to silicon [1]. Similarly, in optoelectronics, there was a transition to GaN for the purpose of general lighting [2]. On the other hand, one could see comparable developments in regard to zinc oxide (ZnO) in the area of wide-band gap semiconductors for optoelectronics [3]. ZnO is considered an oxide semiconductor whose properties come very close to those of GaN. Other applications of GaN include the fabrication of blue LEDs and lasers, among other opto-electronic devices [4]. In the near- and mid-UV regime, however, III-nitride-based LEDs have rather exhibited poor cost and efficiency performance. Currently, the blue or UV-LEDs are fabricated using epitaxial methods like MBE (molecular beam epitaxy) or MOCVD (metal-organic chemical vapor deposition) methods, which incur high manufacturing costs and yield costly products. Compared to conventional LEDs, solution-processed LEDs are relatively inexpensive because they can be fabricated under ambient conditions, which makes any expensive vacuum equipment or conditions unnecessary. Other advantages it offers include the capability of allowing large-scale devices to be fabricated with a process enabling flexible electronics.

Solution-processed ZnO-based LEDs involve nanostructured wide-bandgap semiconductors that open a way into optoelectronics for photodetector [5], LEDs [6], and even lasers [7]. Apart from these applications, ZnO is readily used in photocatalysis [8], storage applications [9], chemical sensing [10], biomarkers [11], and so on. Compared with GaN, ZnO has some advantages for optoelectronic device applications. ZnO is also a compound semiconductor with a direct and wide bandgap of 3.37 eV, comparable to that of GaN; besides, it has an added advantage with a large

free exciton binding energy of 60 meV at room temperature, which is almost 2.4 times larger than that of GaN. This large exciton binding energy of ZnO indicates that efficient exciton emission in ZnO can persist at room temperature and that higher temperatures might yield better light output than GaN. ZnO-based light emitters are expected to exhibit higher efficiency in comparison to GaN-based devices of a similar nature [3]. Also, ZnO is environmentally friendly and readily available as compared to GaN.

Novel methods for generating light using semiconductor nanostructures have arisen and currently garner significant attention. The benefits of nanostructures include a larger junction area, decreased sensitivity to temperature, improved reflectivity concerning polarization, and better confinement of carriers [12]. Semiconductor nanoparticles are considered a promising alternative for the substitution of epitaxial thin film technology, as the synthesis of LEDs employing nanoparticles is affordable and scalable. Nanoscale ZnO has been studied for a very long time, as it is suitable for electronics and photonics applications due to its excellent stability and high electron mobility [13].

These nanoscale ZnO materials have been prepared by various techniques, like chemical methods including sol-gel [14], hydrothermal [15], and precipitation methods [16]. Nonchemical methods include thermal decomposition [17], arc-discharge [18], and RF plasma methods [19]. Generally, ZnO behaves like an n-type semiconductor, due to the presence of native defects like oxygen vacancies and zinc interstitials. Achieving stable and reproducible p-type ZnO is difficult, but important for developing homojunction or heterojunctions and other semiconductor devices. Exploring nanostructures, such as nanoparticles or nanowires, may offer different defect dynamics and may enhance doping control due to its large area-to-volume ratio.

Our group has previously fabricated p-ZnO NPs by arc-discharge and RF-plasma methods and utilized these nanoparticles to fabricate homojunction and heterojunction LEDs [20], [21]. The arc-discharge produces crystalline ZnO NPs without the use of any chemical solvent.

Enhancing the properties of p-type ZnO nanoparticles has posed a challenge in order to boost the power output of LEDs. In order to improve the acceptor nature of ZnO, the fabrication process should be optimized, and the cause of p-character should be identified. Previous research has neither verified the contribution of defects to the p-type nature of ZnO NPs nor studied the relation of acceptor or donor-related properties through the fabrication of LEDs.

Commercial white light is manufactured by introducing a layer of yellow phosphor (Ce: YAG) to blue LEDs. Yellow phosphors use high-energy blue light to undergo a process called down conversion, which results in the emission of lower-energy light waves that occupy the visible spectrum of electromagnetic radiation. Furthermore, the absence of the red component in this white light adversely affects the color rendering capabilities of the white LEDs [2]. UV-LEDs demonstrate better optical stability compared to white light LEDs based on blue light. This is because the variation in optical parameters is minimal, and the variation in the UV regions has less impact on the overall stability than the variation in the blue regions when adjusting the driving current during the calculation of optical parameters [22]. Down-conversion in ZnO-based systems has been achieved in the visible range. Currently, there is no existing report that details the utilization of homojunction ZnO for the production of white light by exciting phosphors. White light has been demonstrated using ZnO, where ZnO NPs act like a phosphor. These NPs absorb high-energy light and convert it into visible light also defect emissions are used to produce white light [23].

Objective of the Study

The objective of this study is to enhance the properties of LEDs by optimizing the synthesis procedure of nitrogen-doped ZnO nanoparticles and assessing the impact of defects in the particles on their p-type characteristics. In addition to these, the final objective of this study is to showcase the feasibility of generating white light emission from zinc oxide-based LEDs.

Outline of the Study

The p-type ZnO NPs are utilized for the production of homojunction ultraviolet light-emitting diodes (UV-LEDs) and the examination of the device's practical uses. To optimize and verify the role of acceptors in p-type ZnO NPs, the fabrication process of ZnO NPs is studied by monitoring the plasma properties during the production of ZnO NPs, which is further supported by the fabrication of LEDs using NPs. However, the fabricated p-type ZnO NPs contain intrinsic and extrinsic defects. The optical properties of the NPs are modified by annealing methods and are studied for acceptor- or donor-related defects in the ZnO. The role of these defects is also studied by fabricating the LEDs. Further mechanisms of defects in nitrogen-doped ZnO NPs are studied in detail.

The application part of the thesis is studied by fabricating full-color electroluminescence-based LEDs from p-type ZnO NPs. The combination of ZnO NPs and phosphors is used to produce a visible LED. White light emission was visualized when the phosphor blend was mixed and applied over the electrode. The thermal effects of LEDs were investigated on aluminum-based LEDs using both current injection and thermoelectric methods. Rendering properties and thermal stability of the emission wavelengths are also studied to understand the optical stability of the LEDs.

The manuscript is organized as follows:

Chapter 1 is devoted to a scientific background. The properties of ZnO are discussed. Further basic mechanisms of light-emitting diodes are discussed. Further, ZnO-based LEDs, including thin films, low-dimensional LEDs and color rendering properties, are reviewed.

Chapter 2 deals with the optimization of the fabrication process of the ZnO NPs using spectroscopic methods. Different conditions of fabrication were monitored using excited-state electron decay signals by optical spectroscopic spectroscopy (OES) techniques and studied for the nitrogen content in the ZnO NPs. Finally, the acceptor-like properties of ZnO NPs were validated by fabricating LEDs and studying the optical properties of the ZnO NPs.

Chapter 3 is devoted to the fabrication and characterization of nitrogen-doped ZnO-NP-based LEDs using spin-coating methods. Initially, the fabrication and characterization of gallium-doped ZnO (GZO) thin film are discussed. Furthermore, ZnO-based LEDs are characterized using *I-V*, electroluminescence (EL), and output power.

Chapter 4 deals with the effect of defects on the acceptor character of nitrogen-doped ZnO NPs and is investigated through the fabrication of NP-based LEDs. ZnO NPs are structurally characterized using X-ray diffraction and scanning electron microscopy. Furthermore, ZnO is optically studied using scanning electron microscopy, Raman spectroscopy, and photoluminescence spectroscopy.

Chapter 5 is devoted to the fabrication of visible ZnO NP-based LEDs using phosphors. The aluminum-based substrate was used to study the effects of heat using the Peltier module. Red, green, and blue light are visualized using phosphors. Furthermore, white LEDs with high color rendering properties are fabricated and presented.

Chapter 6 deals with a summary and recommendations for future work.

Chapter 1. Scientific background

This chapter discusses the properties of ZnO in detail. Additionally, the working principle of LEDs, including both conventional thin film-based and nanostructured ZnO-based LEDs are discussed.

1.1 ZnO properties

A. Physical properties

Zinc oxide is a wide band gap compound semiconductor with a direct band gap of 3.37 eV. ZnO may exist in three different crystal structures: wurtzite-type, cubic zinc blende-type, and rock salt structures. Typically, ZnO solidifies in the hexagonal wurtzite-type arrangement as it is illustrated in **Figure 1**. ZnO has a Wurtzite lattice structure type; its primitive unit cell consists of four atoms. Its space group, P63mc, determines the grouping or the categorization of this lattice type in group theory. According to the JCPDS card 00-036-1451, the ZnO crystal system is hexagonal; the lattice constants are a = b = 3.249 Å and c = 5.206 Å.

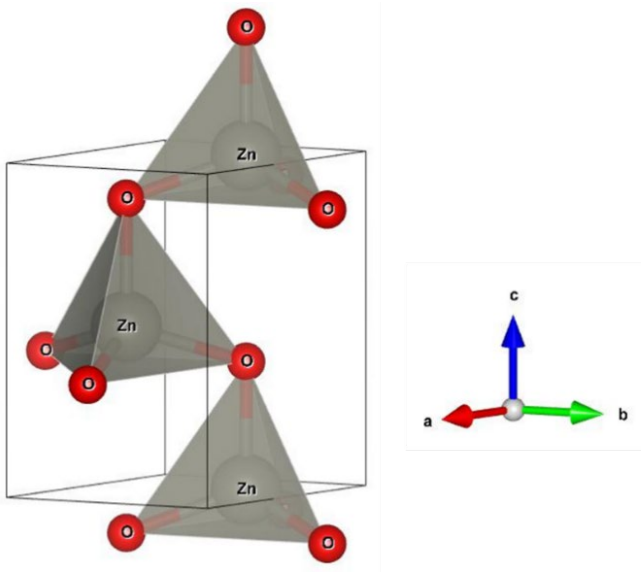

Figure 1. *Crystal structure of ZnO as simulated by VESTA software.*

The number of N = 4 atoms in the unit cell leads to 3 N =12 vibration eigenmodes. Following the rules of group theory, these modes are classified according to the following irreducible

representations: $\Gamma_{opt} = \mathbf{A_1 + 2B_2 + E_1 + 2E_2}$ represents the optical phonon eigenmodes shown in **Figure 2**. The A_1, B_1 $^{(2)}$, E_1, and E_2 $^{(2)}$ modes are oxygen-dominated, and B_1 $^{(1)}$ and E_2 $^{(1)}$ modes are dominated by the Zn-displacement.

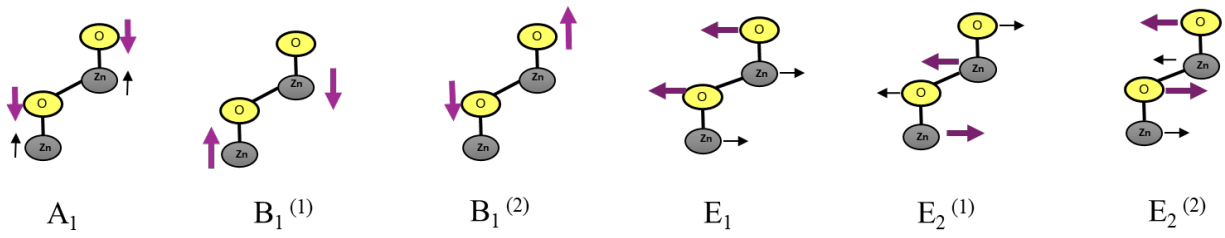

Figure 2. *Eigenvectors of the ZnO optical phonon modes.*

B. Electrical Properties

The electrical characteristics of intrinsic ZnO are similar to n-type semiconductors, due to the presence of inherent defects like vacancies or interstitials. ZnO typically has high electron mobility, 120 - 440 cm^2/Vs which might vary depending upon the growth method, which is beneficial for electronic devices requiring high-speed operation. The carrier concentration of ZnO is around 10^{16} ~ 10^{17} cm^{-3} [24]. The carrier concentration can be significantly enhanced due to doping. ZnO can be easily doped with electron concentrations for n-type semiconductors, but it's very difficult to have stable p-type conductivity due to the compensation nature or low solubility of dopants. Generally, the mobility of the hole is much lower than that of electrons due to the difference in carrier scattering mechanism and effective mass [25].

To fabricate ZnO-based homojunction LED, it's imperative to have both n-type and p-type ZnO. Homojunction LEDs are favored due to fewer lattice strains and can yield better efficiency.

Also, it is important for making commercial LEDs that the doping process be easy and carrier concentrations be accurately controlled.

Doping in ZnO

1. n-type ZnO

Excess electrons doped within a crystal lattice are called n-type ZnO. This type of doping increases electron conduction since there will be a high number of negative charge carriers known as electrons, which lead to the electrical conductivity of the material. Generally, intrinsic ZnO exhibits n-type conductivity because of inherent defects, mostly oxygen vacancy (V_O), zinc antisite (Zn_O), zinc interstitial (Zn_i), and/or hydrogen incorporation. Interstitial hydrogen (H_i) or substitutional hydrogen (H_o) could impact increasing the donor concentration of the n-ZnO [26], [27]. Look *et al.* proposed that Zn_i, instead of V_O, is the prevailing indigenous shallow donor in ZnO materials [28]. Mitra *et al.* investigated the role of zinc interstitials and their complexes with oxygen vacancies could impact n-type ZnO [29]. Intentional n-type doping has been achieved by using group III elements as dopants, such as In [30], Ga [31], and Al [32], which can easily replace Zn ions, improving the donor concentration. Moreover, group VII elements such as Cl and F can also be used to substitute oxygen to impart n-type properties [33].

2. p-type ZnO

The process of p-type doping of ZnO, which is essential for fabricating LEDs, is challenging and is considered a barrier to the use of ZnO-based materials for light-emitting applications as ZnO inherently acts as an n-type semiconductor and p-ZnO suffers from issues including deep acceptor energy levels, low solubility of acceptor dopants, and self-compensating parameters. Therefore, to grow p-type ZnO, the concentration of acceptors must exceed the concentration of unintentional donors. Thus, for effective doping, the acceptor energy level should become shallower, dopant solubility should increase, and finally, the self-compensation effect due to donor effects should be

reduced [34]. Intentional doping can be achieved by some methods, like substituting Zn sites by group I dopants, substituting O sites by group V dopants, or by codoping.

Group I doping

Substituting group I elements (Li, Na, and K) for Zn sites may enable p-type doping in ZnO. Battagin *et. al.* studied the Li-doped ZnO-based thin film [35]. The ionic radius of sodium is larger and closer to that of zinc compared to lithium, introducing sodium to replace zinc in the ZnO lattice will result in less lattice distortion. Thus, Na is more likely to form an acceptor [36]. Cu and Ag have also shown some promising examples [37], [38].

Group V doping

The group V elements (N, P, As, and Sb) have long been considered the most promising dopants for p-type ZnO. Aoki *et al.* used Sb as a dopant source in ZnO by excimer laser irradiation to form p-ZnO [39]. As is also used as a dopant in p-ZnO by the simple diffusion method [40]. P is also used to p-type ZnO by MOCVD [41]. Among all the group V elements, nitrogen is considered one of the best dopants for replacing oxygen sites due to its similar atomic radii [42], [43].

Co-doping

Co-doping the donor and acceptor can increase the incorporation of the acceptor while simultaneously decreasing the binding energy of acceptor impurities. Yamamoto studied the co-doping effect of the N acceptor with Ga and produced low-resistive p-ZnO films [44].

1.2 Light-emitting diodes (LEDs)

Generally, holes and electrons in semiconductors combine to either radiatively emit photos or non-radiatively emit phonons upon current injection. Radiative recombination is necessary for better light efficiency than non-radiative recombination. Employing the principles of

electroluminescence and semiconductor physics, LEDs promise several advantages over traditional sources of light: improved energy efficiency, long service life, high switching speeds, and flexibility in design.

The LEDs typically work in forward-biased conditions in which the radiative processes are dominant. The voltage induces an electric field that promotes the migration of electrons from the n-type to the p-type region, and the migration of holes from the p-type to the n-type region. Electrons and holes undergo recombination at the interface between the p and n regions as they traverse the junction. Typically, the majority of electrons from the n-type layer are transferred to the p-type layer due to the significantly greater electron mobility. Recombination of the electron and hole may lead to radiative loss or non-radiative loss of energy. If the dissipation of energy is in radiative, then light is emitted or in the case of non-radiative recombination, heat is released. This radiative recombination process gives LEDs their ability to emit light. The released energy corresponds to the bandgap of the semiconductor material that makes up the LED. The principle of band diagram under zero bias and under reverse bias is shown in **Figure 3**.

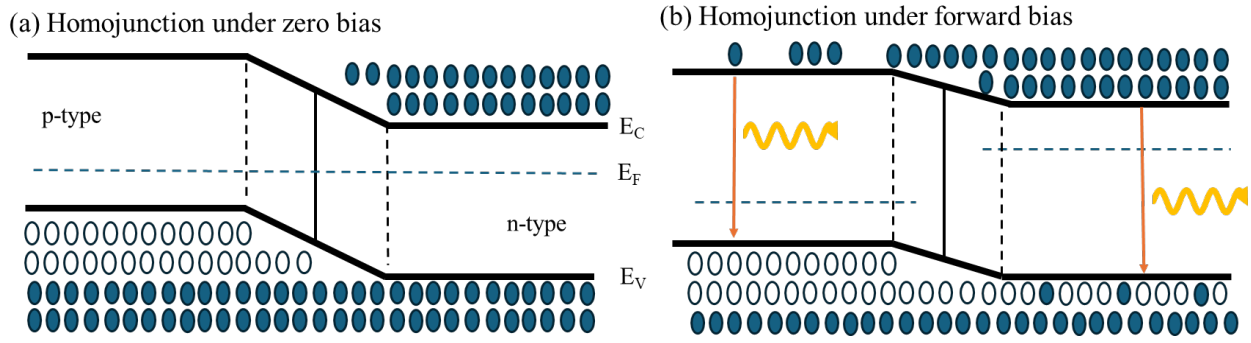

***Figure 3**. Band diagram of p-n homojunction. (Ref 52)*

LEDs only operate when forward biased; when the diode is reverse biased, meaning that the cathode is positive in relation to the anode, the diode prevents the flow of current except for a very

minimal amount of leakage current. Luminescence occurs in the diffusion regions of p-type and n-type carriers.

The device's ohmic or rectifying behavior of the diode can be monitored using *I-V* characteristics. The diode's *I-V* characteristics can be modelled by the non-linear Shockley diode equation. The Shockley diode equation essentially describes the exponential relationship between diode current and voltage.

$$I = I_s\,(e^{qV/kT}-1)$$

Where I_s is the saturation current. Under typical forward bias conditions, diode voltage $V >> kT/e$ thus ($e^{qV/kT}$-1) can be approximately equal to $e^{qV/kT}$. Thus, diode current I can be written as $I = I_s$ ($e^{qV/kT}$). Oftentimes, a diode exhibits undesired or parasitic resistances and can be used to diagnose potential issues with *I-V* characteristics. The original Shockley diode equation has a diode ideality factor of $n_{ideal} = 1$. The Shockley diode equation is generally modified to include an "ideality factor". Diode current, I directly proportional to $\exp(eV/n_{ideal}kT)$.

1.3 ZnO based LEDs

A. Heterostructure LEDs

Through the use of n-ZnO and most commonly used p-type materials, it is easier to make ZnO-based heterostructure LEDs. This would avoid the problem associated with obtaining p-ZnO. The most commonly investigated structure for the hetero-structure is n-ZnO grown on p-ZnO [45]. Yuen *et. al.* fabricated pn-junction by depositing n-ZnO on p-SiC at low temperatures [46]. Baltakesmez *et. al.* fabricated LED and UV-visible detectors on p-Si by depositing n-ZnO by electrochemical techniques [47].

B. Homojunction LEDs

An LED with a homojunction is consistently favored for its superior light-emitting efficiency when compared with heterostructures because the lattice strains are minimal within the same material and yield better efficiency. Violet electroluminescence was detected from the homojunction LEDs utilizing nitrogen as the dopant [6]. Al–N-co-doped ZnO-based homojunction LED was fabricated by sputtering with low leakage [48]. Blue electroluminescence was observed from the LEDs with a p-i-n structure [49]. Generally visible emission is observed from ZnO-based homojunction LEDs, which come from the defect luminescence of ZnO. Near-band edge UV emission from the ZnO was observed with nitrogen as a dopant, indicating hole injection from p-ZnO to n-ZnO [50].

1.4 ZnO-based nanostructure LEDs

The high surface-to-volume ratio of nanostructures can incorporate dopants with high concentration without affecting their performance. This makes it a prominent method for doping ZnO nanostructures. ZnO with reduced dimensions has been extensively employed in various optoelectronics applications like LEDs or Lasers. UV emission was observed in ZnO-based nanoparticles [20] and nanowires [51].

1.5 White light and color rendering

Visible wavelengths range from 380 – 770 nm. At the boundary of the wavelength range 380 nm (near-UV) and 770 nm (near-IR), eye sensitivity is not high enough, leading to inaccuracies. The human visual system is typically more responsive to the color green. Light stimulates different levels of activation in the green, blue, and red photoreceptor cells in the eyes. The International Commission for Illumination (CIE 1931) has established guidelines for color measurement using the chromaticity diagram and color matching functions in order to ensure standardization [52]. The color of a light source can be precisely described using three variables known as color matching

functions $\bar{x}(\lambda)$, $\bar{y}(\lambda)$ and $\bar{z}(\lambda)$. For a given power spectral density $P(\lambda)$, the color of $P(\lambda)$ is given by three equations based on three tristimulus values X, Y and Z [52].

$$X = \int_{\lambda} \bar{x}(\lambda)\, P(\lambda)\, d\lambda$$

$$Y = \int_{\lambda} \bar{y}(\lambda)\, P(\lambda)\, d\lambda$$

$$Z = \int_{\lambda} \bar{z}(\lambda)\, \mathrm{P}(\lambda)\, d\lambda$$

The color coordinates x and y were subsequently computed based on these values using mathematical equations.

$$x = \frac{X}{X + Y + Z}$$

$$y = \frac{Y}{X + Y + Z}$$

$$z = \frac{Z}{X + Y + Z} = 1 - x - y$$

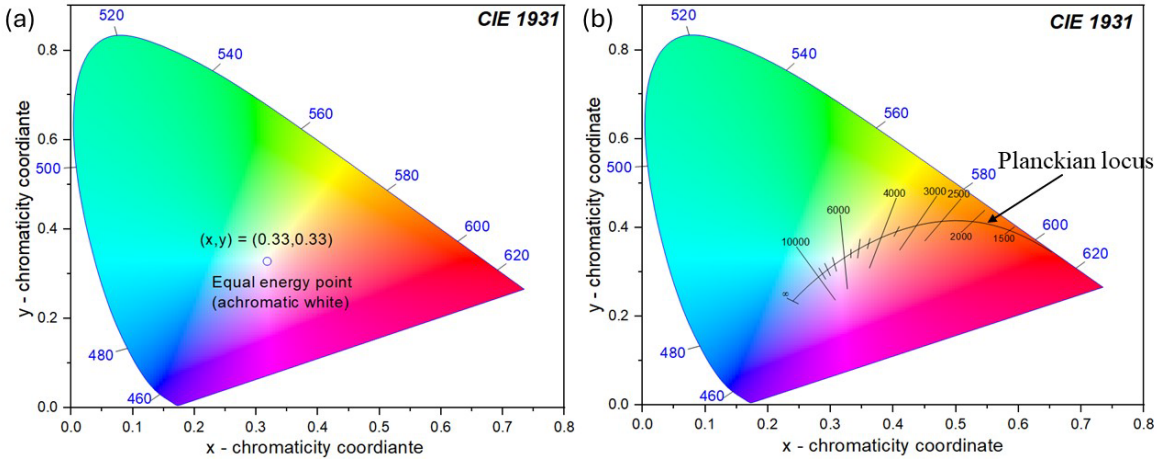

Figure 4. (a) *Chromaticity chart 1931 depicting qual energy point* ***(b)*** *Planckian locus. (Ref 52)*

Monochromatic colors are located along the outer edge of the chromaticity diagram. The chromaticity diagram features a central region in its middle section that corresponds to the location of white light. The achromatic white light is referred to as the light of the equal energy point because its tristimulus values, represented by the coordinate (*x,y*) = (1/3,1/3), are equal, as depicted in **Figure 4a**. The location of the black-body radiation on the chromaticity diagram is known as the Planckian locus, as shown in **Figure 4b**. The black-body spectrum is defined by the equation.

$$I(\lambda) = \frac{2hc^2}{\lambda^5 \left[\mathrm{e}\left(\frac{hc}{\lambda kT}\right) - 1\right]}$$

Where *I* is the intensity of the light coming out which is the black body radiation as a function of wavelength, λ. Color temperature refers to the temperature of a Planckian black-body radiator that has the same chromaticity location as the white light source being measured. This correlated color temperature is used whenever the chromaticity co-ordinate of a white light source lies apart from the Planckian locus on the chromaticity diagram [52].

Color rendering describes the capacity of a source of light to accurately reproduce the colors of objects as if they would have appeared in natural sunlight. This can be achieved by replicating precisely the whole range of wavelengths of light constituting all the colors in the spectrum. In doing this, balanced spectral power distribution should, therefore, be maintained as most similar to that of the sun. Although sunlight is generally accepted as the best standard of color accuracy, all other artificial light sources, under which colors cannot often be correctly represented with respect to brightness, hue, and color accuracy.

Conventionally, the Planckian black-body reference source is considered to possess good color rendering properties, with a color rendering index (CRI) of 100, as it closely resembles sunlight. A light source with a CRI index of 100 can provide the best color rendition only. The incandescent

quartz halogen lamps very closely duplicate the characteristics of a Planckian black-body radiator. They possess a CRI of the highest possible, making them the most efficient artificial light source which provides the most accurate colors to the objects. The disadvantage is that these bulbs are inefficient and consume a significant amount of power. Therefore, LEDs would have a pivotal role in energy consumption.

Basically, there are two common approaches to generating white light based on phosphors. The first and most common approach is exciting the yellow phosphor with a blue LED, and the second is exciting blends of phosphors using UV or blue light. The first approach is commercially used as it is a low-cost-intensive process in which GaN-based blue LEDs use yellow phosphor, usually made up of YAG:Ce, to cover the blue and yellow regions of the spectrum to make white light. This approach also suffers from weakness, as it has a poor color rendering index and low stability of color temperature. The latter approach solves the aforementioned pitfalls but can have complex fabrication processes.

ZnO based White LEDs

In order to have optically stable white LED, phosphors blends should be excited by high energy UV light. ZnO based UV-LED can be used to do the same. Previously, the broad emissions from the defect's parts of ZnO has be utilized for the white emissions. Near band excitation of the phosphors using ZnO have been only demonstrated in the visible regions. No reports are available for the white emission by band-edge excitation process for ZnO.

Chapter 2. Preparation and characterization of p-type ZnO nanoparticles (NPs)

Synthesis of nitrogen-doped ZnO NPs was prepared with the help of the arc discharge method, while characterization has been carried out using optical emission spectroscopy and photoluminescence spectroscopy. A study of the structural properties has been performed on ZnO NPs with X-ray diffraction and electron microscopy methods in this paper.

In this chapter, the results of the optimization of ZnO NPs' fabrication process through the spectral analysis of plasma formed during the process of arc discharge are presented. Furthermore, the fabrication of NP-based LEDs was done in order to investigate the acceptor dopants of ZnO, relating them to nitrogen concentration in the ZnO NPs.

2.1 Preparation of ZnO NPs

An arc discharge device, which is shown schematically in **Figure 5**, was used to synthesize p-type nitrogen-doped ZnO NPs. The arc current can be adjusted from 10 to 100 A. With compressed gas, the chamber pressure can be adjusted within the range of 10 to 760 Torr and gas flow up to 20 L/min in conjunction with a vacuum pump.

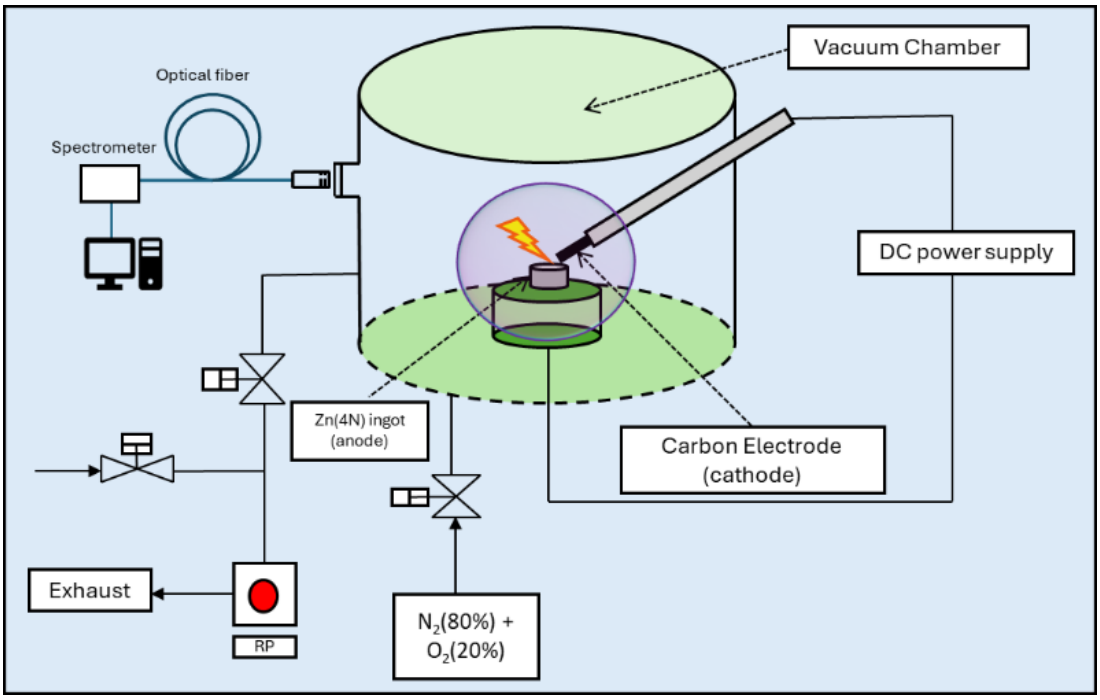

***Figure 5**. Schematic diagram of arc discharge apparatus. (Ref 55)*

In the arc discharge process, the discharge occurs between the cathode and anode, as shown in **Figure 6**. Zinc ingot is employed as the anode material, while a carbon electrode is used as the anode in the arc discharge equipment. The zinc ingot was prepared from a zinc wire that is 99.99% pure. This wire is cut into several small pieces, about 5 mm in length and 3 mm in diameter. An automated heater is specially designed to heat and cool these thin wires according to a pre-programmed system, and with time changes, it gradually transforms them into a firm zinc ingot inside a ceramic container. In the beginning, the heater's temperature is rapidly increased from room temperature to 750°C for 12 minutes, then cooled to 700°C for another 12 minutes, 450°C for 9 minutes, 300°C for 6 minutes, and 150°C for 6 minutes before being gradually lowered to room temperature. Finally, a truncated cone-shaped Zn metal block is obtained. This multiple-step

process of heating and cooling leads to a firm zinc ingot that can withstand the impact of electron knocking.

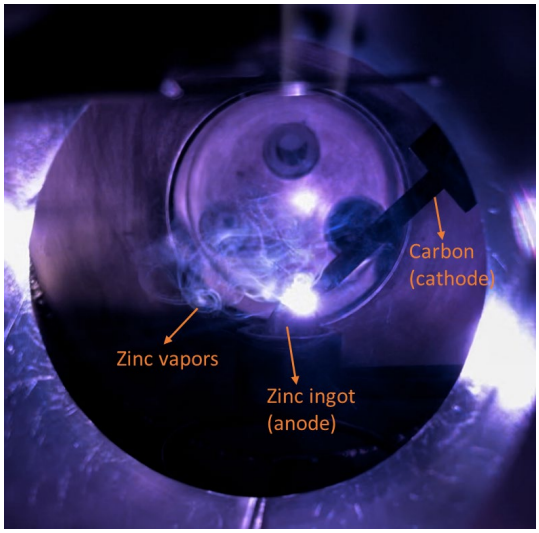

***Figure 6**. Arc discharge process. (Ref 73)*

Direct current (DC) oxidizes zinc to form ZnO NPs inside the plasma chamber when pure O_2 and N_2 gas are combined while maintaining a cathode–anode separation close to 1 mm, as shown in **Figure 7a**. A valve linked to the vacuum pump was used to control the chamber pressure. A mixture of pure N_2 and O_2 was introduced into the chamber at a ratio of 4:1. A constant DC was maintained between the anode and cathode, which formed gas plasma as well as zinc plasma. The zinc plasma was oxidized into ZnO NPs inside the chamber by vapor condensation technique. In this technique, zinc vapors were quicky quenched via the condensation method by interacting within the cooler regions of the arc discharge chamber.

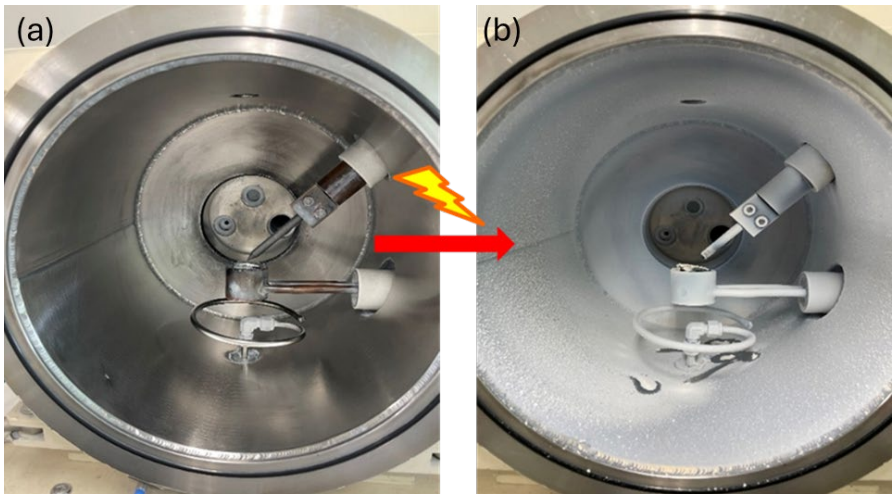

***Figure 7**. Chamber **(a)** before and **(b)** after arc discharge. (Ref 55)*

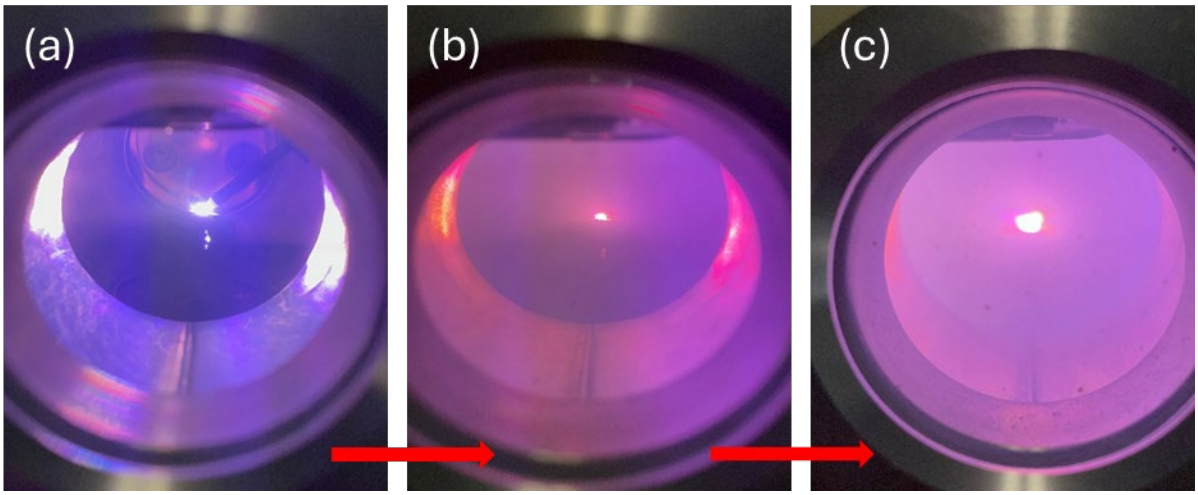

***Figure 8**. Plasma state while fabrication of ZnO NPs.*

By varying the arc current between the zinc metal ingot (anode) and the sharp part of carbon (cathode), the high electric field was maintained in the gas (a mixture of O_2 and N_2). Plasma is formed when an electric current passes through the gas. When the voltage became larger than that needed to ionize, the free electrons started to accelerate and collided with the gas molecules, breaking off their loosely held electrons, forming thus a pair of one free electron and a positively charged gas ion. Consequently, the ionization of the arc discharge is observed as a purplish glow, seen in **Figure 8a**. A few gas molecules and Zn metal near the arc discharge ionize as the electric field rises, while the rest of the surrounding gas remains near room temperature. The plasma color

changes to a reddish hue as the red light is scattered by small particles, as seen in **Figure 8b**, and slowly changes to white as the particles increase in size, as seen in **Figure 8c**. The ionized gases produced in an arc discharge are accelerated by an electric field and combined with the incoming cooled gas (a mixture of O_2 and N_2) to form ZnO nucleases, the particles will grow into nanorods or nanoparticles when they collide with the cooled walls of the plasma chamber and cool down quickly as shown in **Figure 7b**. Homogeneous nucleation occurs when ultrafine particles are formed due to the vapor species becoming supersaturated as a result of rapid cooling. ZnO nanostructure formation is highly favorable for ZnC, ZnH, and Zn_3N_2, because Zn^{2+} has a substantially higher electron affinity for oxygen than C, H, and N [53].

The morphology and size of nanostructures depend on various factors, such as plasma expansion plasma ablation, and convective condensation. To fabricate p-type ZnO NPs, the total chamber pressure was maintained at approximately 150 Torr at a constant flow rate of 5 L/min, and the arc current was varied from 20-60 A. Generally, when plasma is scattered and cooled under non-equilibrium conditions results in the interaction of plasma components and the creation of clusters and NPs. The NPs are further characterized to study their structural and optical properties.

2.2 Characterization of ZnO NPs

The plasma parameters change while NPs are being generated as the distance between the cathode and anode changes during consumption. Also, plasma parameters depend on current density. Thus, the characterization of plasma was important to study to optimize the fabrication process.

2.2.1 Optical Emission Spectroscopy (OES)

OES is a very powerful tool of analytical technique to identify and quantify the elements within a sample, according to the various wavelengths of light which atoms or ions emit in the sample while excited. Generally, in OES, the samples are excited by high-energy sources, which causes the

excitation of ions or atoms to higher energy levels. Energy is released in the form of light when the excited elements return to their ground state. This light energy can be segregated by the help of spectrometers using interference techniques. Further results can be studied to identify the elemental composition precisely.

In our arc-discharge setup, a similar analysis is being performed to study the decay of electronically excited-state molecular and atomic species in the fabrication process. Saji *et. al.* studied similar kinematics and characterized a ZnO-based ablation plume by laser through optical emission spectroscopy [54].

The Ocean Optics QE65000 scientific-grade spectrometer, which has a wavelength range spanning from 200 to 1000 nm with an optical resolution of 0.14 nm full width at half maximum (FWHM), was employed to capture the optical emission spectra emitted by the arc plasma. The distance between the optical fiber and quartz window was kept constant, as shown in the experimental setup in **Figure 9** to maintain constant plasma parameters. The output data were gathered with an integration time of 1 s. A standard tungsten halogen standard light source (LS-1-CAL) was further used to calibrate the spectra. Using OES, the decay of electronically excited state molecular and atomic nitrogen, carbon, and oxygen, in addition to zinc metal vapor was observed in the dc arc plasma as a function of chamber pressure and plasma density, which are controlled by the breakdown voltage of the dc circuit.

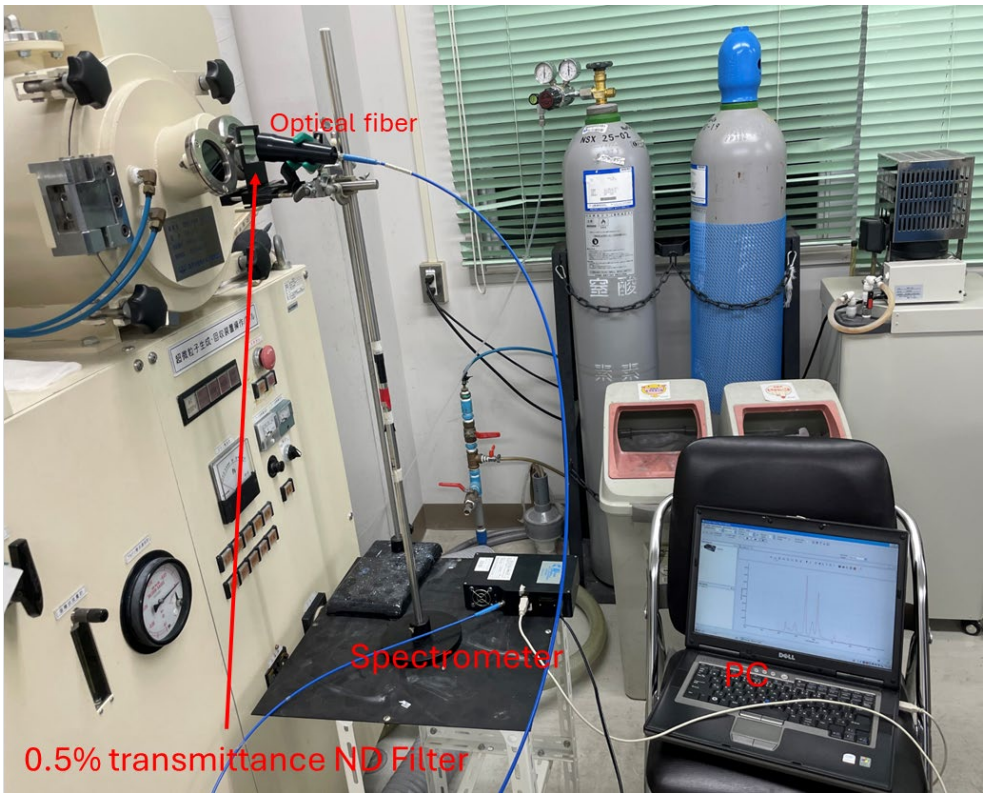

Figure 9. *Optical emission spectroscopy measuring setup.*

Figure 10 represents the OES spectra during the synthesis of ZnO NPs at a chamber pressure of 150 Torr with a function of arc current (20 A ~ 60 A). The excited state electron decay signals were recorded by OES in the arc plasma. This region contains both neutral and singly ionized zinc lines, as well as nitrogen and oxygen radicals. The optical transition observed at 468.2, 472, 481, 636.1, and 692.4 nm is arising from neutral zinc. The zinc spectral line at 328.2 nm corresponded to the $4s4d\ ^3D_1 \rightarrow 4s4p\ ^3P_1$ transition, the line at 468.0 nm corresponded to the $4s5s\ ^3S_1 \rightarrow 4s4p\ ^3P_0$ transition, and the line at 472.2 nm corresponded to the $4s5s\ ^3S_1 \rightarrow 4s4p\ ^3P_1$ transition. Among these emission lines, the most intense emission at 636.1 nm corresponds to the autoionization of inner d-shell electrons and their possible transitions. The atomic oxygen O(I) transition is observed at 777.1 nm [55].

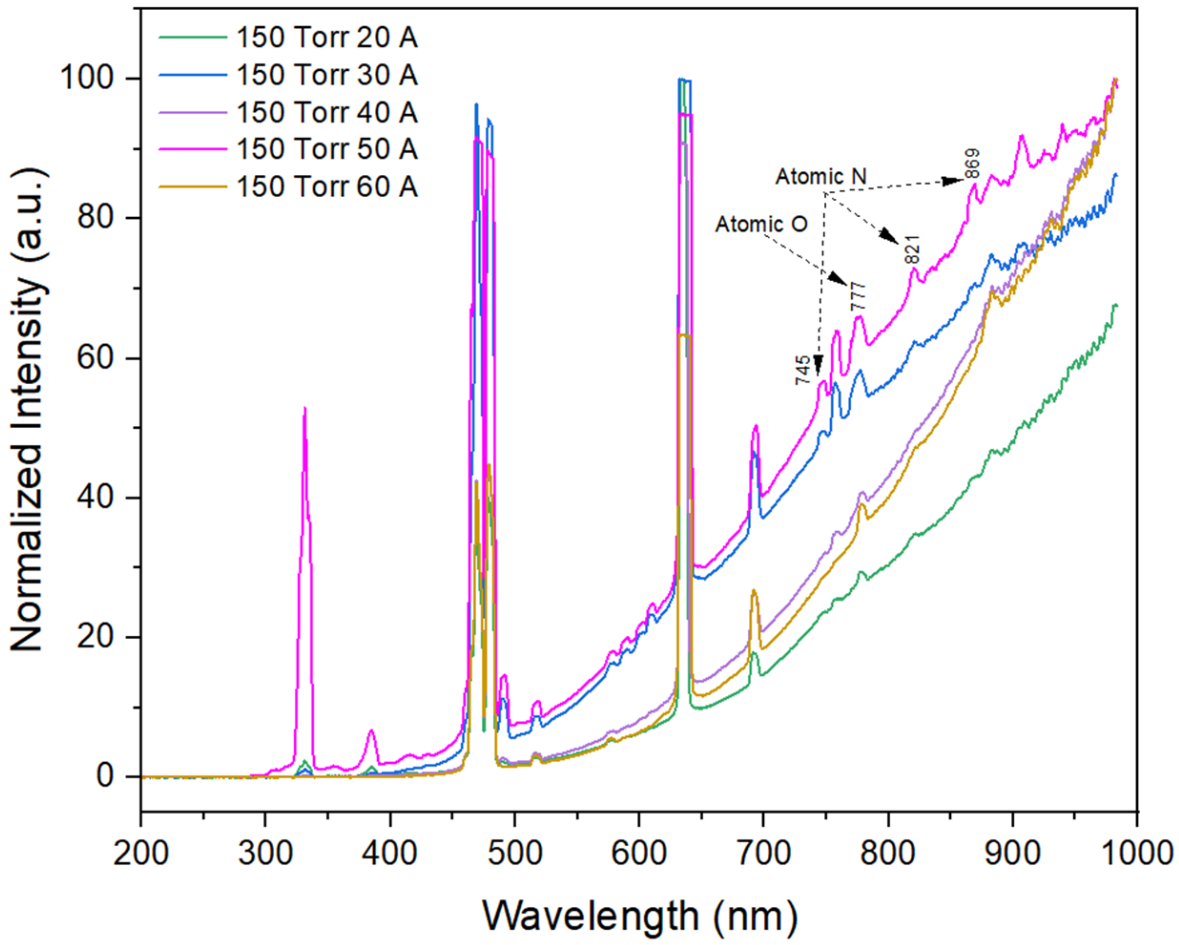

***Figure 10**. OES spectra during synthesis of ZnO NPs at the chamber pressure of 150 Torr with a function of arc current (20 A ~ 60 A). (Ref 55)*

The discharge's high energy causes the gases to dissociate into plasma. The dissociation reaction of the mixture of gas plasma is given in the following steps [56]-

$$O_2 + e \rightarrow 2O^* + e$$

$$N_2 + O^* \rightarrow NO + N^*$$

$$NO + e \rightarrow N^* + O^* + e$$

The O(I) transition occurred at a wavelength of 777.1 nm, while emissions from N atoms were detected at wavelengths of 745, 821, and 869 nm using OES. Other optical transitions that are present in **Figure 10** have been previously identified. Kumar *et. al.* also observed optical

transitions from the CN radical violet system at around 385 nm when the chamber pressure was decreased [57].

At the chamber pressure of 150 Torr and current of 50 A, the highest intensity of the N emission is observed when compared with other fabrication conditions. When the chamber pressure increases to 610 Torr, the intensity of the N emission decreases, as shown in **Figure 11**. Thereby indicating less nitrogen content as the chamber pressure increases.

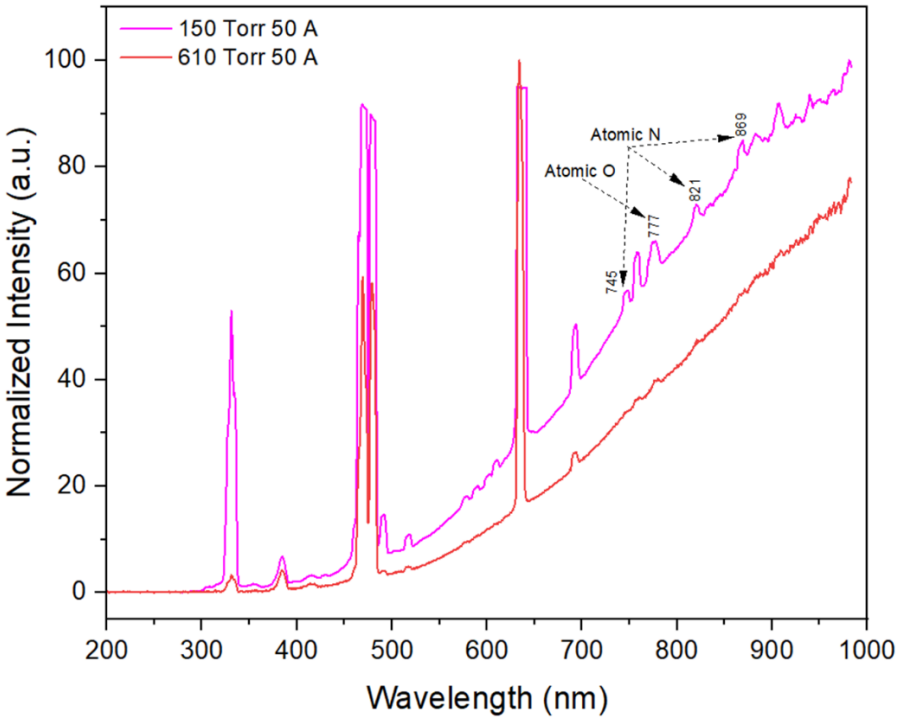

***Figure 11**. OES spectra during synthesis of ZnO NPs at the chamber pressure of 150 Torr and 610 Torr and an arc current of 50 A. (Ref 55)*

2.2.2 Nitrogen concentration

The nitrogen concentration of prepared ZnO nanoparticle samples was determined using a thermal conductivity detector (Horiba EMGA-830). **Figure 12** shows the nitrogen concentration of ZnO NPs fabricated with a chamber pressure of 150 Torr as a function of arc current (20 A ~ 60 A). ZnO NPs fabricated with a chamber pressure of 150 Torr and arc current of 50 A showed the

highest nitrogen content when compared to other fabrication conditions. It should be noted that the nitrogen concentration, as determined by the thermal conductivity method, included nitrogen molecules that were absorbed on the surface.

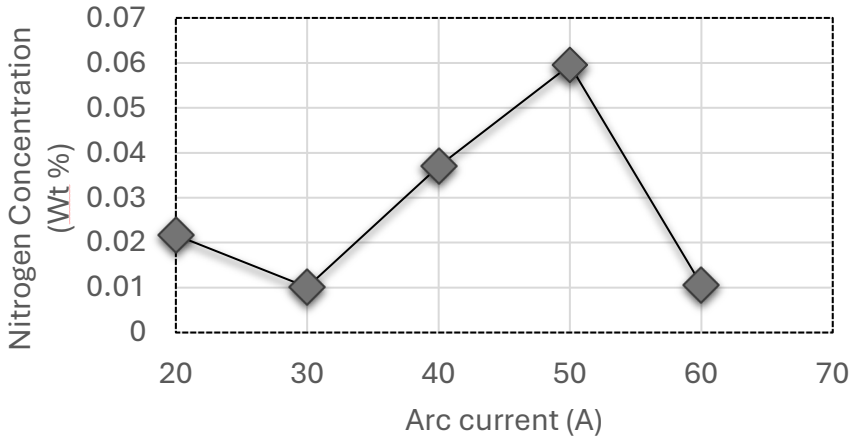

***Figure 12**. Nitrogen concentration of ZnO NPs fabricated with a chamber pressure of 150 Torr as a function of arc current (20 A ~ 60 A).*

2.2.3 Plasma Temperature

Plasma temperature is one of the important parameters; it could be used for studying plasma characteristics formed and optimization of the process. Plasma temperature is kinetic energy considered as the mean of the energy of electrons in plasma. Inside the plasma, electrons show very high energy levels, and their velocities follow the Maxwellian distribution. The electron temperature signifies the mean energy of electrons within this distribution. It quantifies the amount of thermal energy that the electrons in plasma possess.

The electron temperature was calculated using the ratio of the relative intensity ratio of Zn(I) (481.4 and 636.1 nm in the OES) by the following relation, as shown in the equation-

$$\frac{I_1}{I_2} = \frac{g_1 A_1 \lambda_2 \, \mathrm{e}^{-E_1/kT_e}}{g_2 A_2 \lambda_1 \, \mathrm{e}^{-E_2/kT_e}}$$

In this equation, the subscripts 1 and 2 denote the two spectral lines originating from the identical element. The spectroscopic constants I_i, λ_i, g_i, A_i, *and* E_i *(i = 1, 2)* correspond to the line intensity, wavelength, statistical weight, transition probability, and energy of the excited state, respectively. T_e and k are the electron temperature and Boltzmann constant, respectively. The two emission lines of Zn(I), $4s5s\ ^3S_1 \rightarrow 4s4p\ ^3P_2$ at 481.05 nm and $4s\ 4d\ ^1D_2 \rightarrow 4s4p^1P_1$ at 636.2 nm, were used to determine the electron temperature under the condition of local thermodynamic equilibrium (LTE) [58]. The spectroscopic constants for these transitions are mentioned in **Table 1** and are used to calculate the electron temperature of the plasma.

Table 1. *Spectroscopic parameters of the neutral zinc (Zn I) lines. (Ref 55)*

Wavelength λ (nm)	Transitions	Statistical Weight (g_k)	Transition probability A(s^{-1})	Excitation energy E (cm^{-1})
481.05	$4s5s\ ^3S_1 \rightarrow 4s4p\ ^3P_2$	3	7.00 X 10^7	53,672.24
636.23	$4s\ 4d\ ^1D_2 \rightarrow 4s4p^1P_1$	5	4.65 X 10^7	62,458.51

The correlation between the plasma temperature and nitrogen content of the NPs, as shown in **Figure 13**. The plasma temperature exhibited a high level during the initial phase of discharge and subsequently reached a state of saturation at a low value. Plasma expansion rapidly converts thermal energy into kinetic energy, resulting in a decrease in temperature. The rapid reduction in plasma temperature can be accounted for the conversion of thermal energy into kinetic. ZnO NPs when fabricated at chamber pressure of 150 Torr and 50 A resulted in the lowest plasma temperature among all the conditions. The rapid expansion of plasma at an elevated current density is thermalized due to the energy transfer to its surroundings. The atomic nitrogen intensity at the 869 nm line exhibited an increase from 150 Torr (from 20 A to 50 A), as shown in **Figure 10**, to a

maximum at 150 Torr and 50 A, which agreed with the nitrogen concentration measured from the inert gas method.

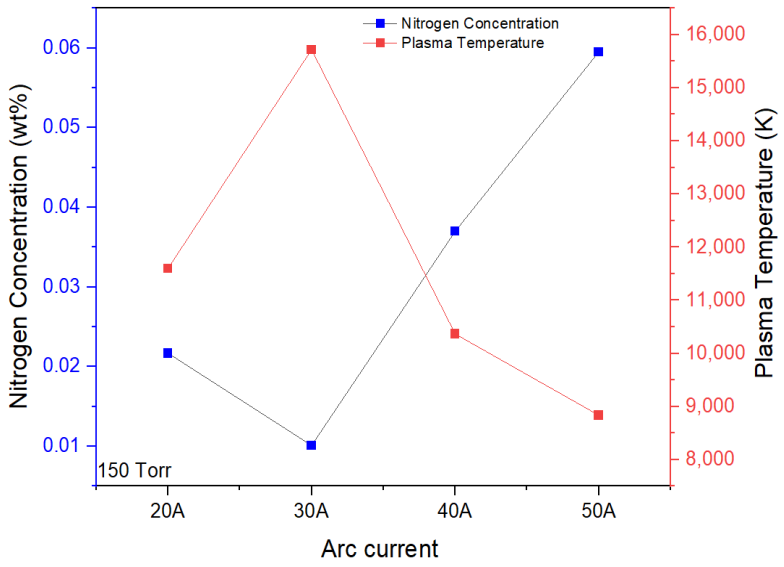

***Figure 13**. Relationship between nitrogen concentration and Plasma temperature. (Ref 55)*

2.2.4 Photoluminescence (PL)

The PL spectrum measured the optical properties of ZnO NPs at room temperature. Any semiconductor material having energy greater than its band gap can ignite electrons from the valence band to the conduction band by photons. Electrons in the conduction band of ZnO combine with holes in the valence band, releasing photons. PL was conducted by exciting weak-intensity UV light (325 nm) from the Xenon lamp, which resulted in the emission spectrum. This emission spectrum consisted of broadly two peaks, one sharp peak (near UV region) and one broad peak (near visible region). The exciton binding energy lies 60 meV below the conduction band and corresponds to the transition of free excitons in ZnO.

The interaction between donor and acceptor impurities in ZnO can result in the formation of donor-acceptor pairs. Donor–acceptor-pair (DAP) luminescence provides a direct method for studying the involvement of acceptors in ZnO. The role of nitrogen as an acceptor in the ZnO can be studied

by the deconvolution of the PL spectra at the near-band-edge (NBE) emissions of the ZnO indicating the DAP luminescence. Zeuner et al. discovered that the energy level ZnO donor–acceptor-pair (DAP) band was found to have a zero-phonon line at 3.235 eV, regardless of whether the samples were pure or nitrogen-doped. Additionally, a phonon replica was detected within the energy gap, measuring approximately 72 meV [59]. Chen et. al. examined the process of the free exciton (FX) recombination. They found that the emission near the band edge at 3.289 eV is the most prominent in the spectra of nitrogen-doped ZnO at room temperature. The transition of an electron from the conduction band to an acceptor energy level (FA) was reasonably assigned a value of 3.241 eV [50].

The exciton and DAP emissions of the deconvoluted NBE emissions are shown in **Figure 14**. Since the rise in DAP intensity goes with the rise in nitrogen concentration, it suggests that nitrogen atoms are present, hence verifying the claim that nitrogen acts as an acceptor. ZnO NPs fabricated at a chamber pressure of 150 Torr and a current of 50 A, resulted in the maximum DAP luminescence, which is further supported by the maximum incorporated nitrogen as calculated by thermal methods.

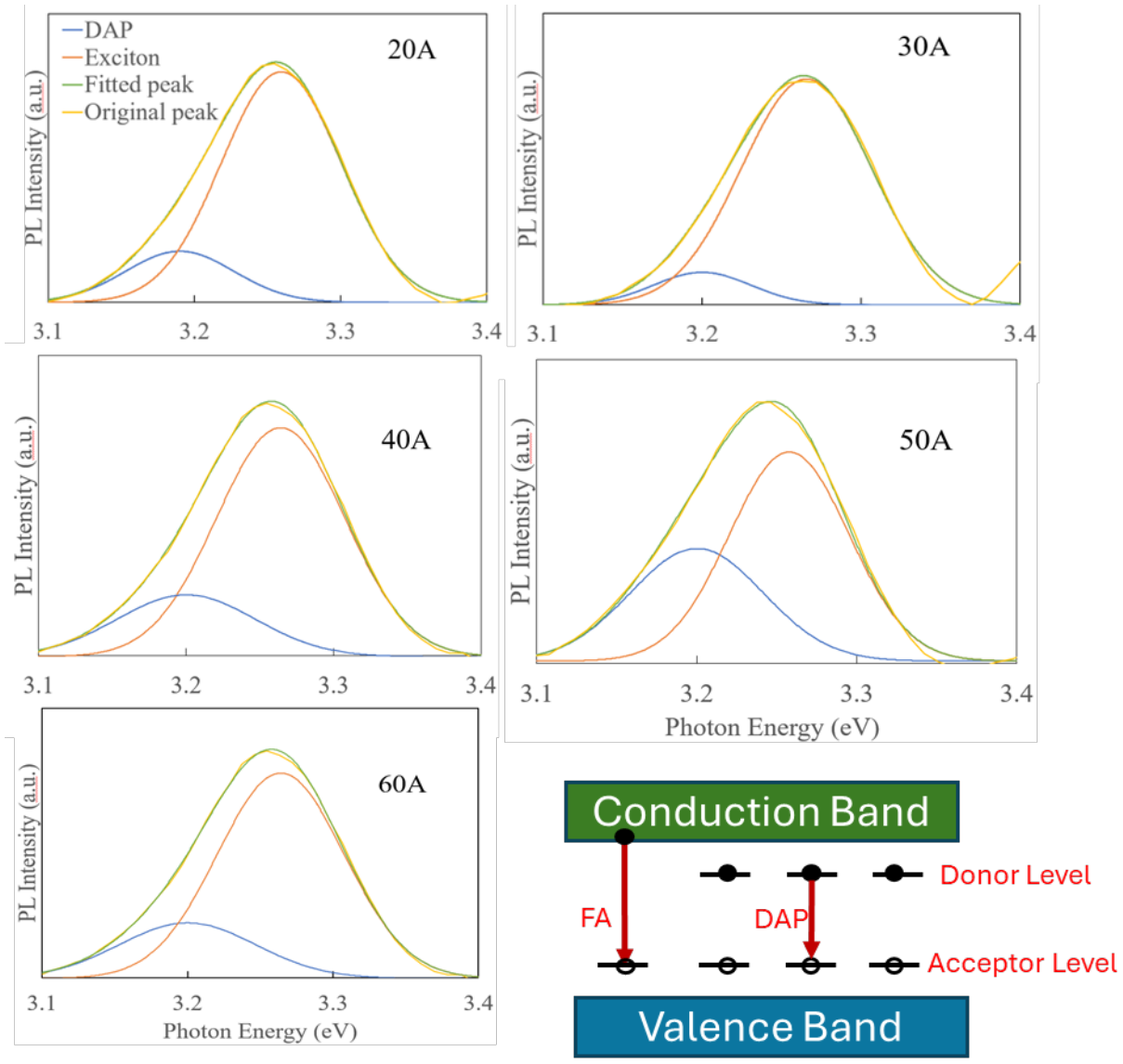

Figure 14. *Deconvoluted PL emissions of near-band-edge emission regions. (Ref 55)*

2.3 Conclusion

In this chapter, the preparation and characterization of ZnO NPs are discussed. The fabrication conditions of ZnO are studied by plasma parameters through optical emission methods. Further, the NPs were optically characterized using PL and correlated with the nitrogen concentration and the DAP luminescence.

Chapter 3. Fabrication and characterization of nitrogen doped ZnO NPs based LEDs

3.1 LED fabrication process

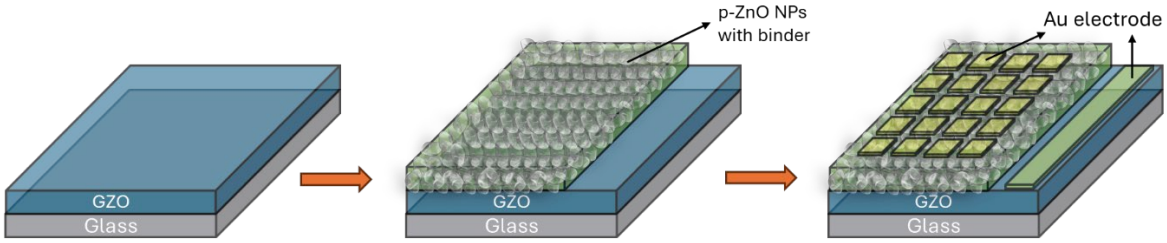

Figure 15. *Schematics of LED fabrication. (Ref 67)*

A p-ZnO layer was fabricated on the sputtered GZO (gallium-doped ZnO) layer by spin-coating for the homojunction LED.

3.1.1 GZO formation

Initially, an n-type gallium-doped ZnO (GZO) layer was deposited onto a flat glass substrate using radio frequency (RF) magnetron sputtering. The RF power supply was around 200 W. The separation between the target and substrate was fixed at 15 cm. The sputtering target comprised ZnO/Ga_2O_3 (5 at. %). The deposition chamber pressure was initially evacuated to less than 1×10^{-6} Torr. High-purity Ar was used as the sputtering gas. The substrate angular speed and temperature were maintained at 1 rpm and 300 °C, respectively. Prior to depositing the GZO thin film, the target underwent pre-sputtering in an Ar atmosphere for approximately 10 minutes to eliminate the oxide layer on the surface. The thickness of the sputtered GZO was determined using the optical interference method with a NanoCalc-2000-UV/VIS/NIR instrument. **Figure 16a** displays the UV-Vis optical transmittance spectra of the GZO films that were formed on the glass substrate. The UV/Vis optical transmission statistics from the 200-1100 nm wavelength range show outstanding transparency, with a transmission percentage of more than 90% in the visible

region and around 80% in the near-UV region. The deposited GZO films on the glass substrate are very transparent to visible light, allowing for clear visibility of the university logo, as shown in the inset of **Figure 16a.** The observed interference fringes from the transmission spectra feature tall crests and deep valleys, indicating a smooth surface on the film [60]. The room temperature UV-visible spectrum of the as-prepared Ga-doped ZnO thin film exhibits a strong absorption band-edge around 300 nm, which is blue-shifted due to the high electron concentration.

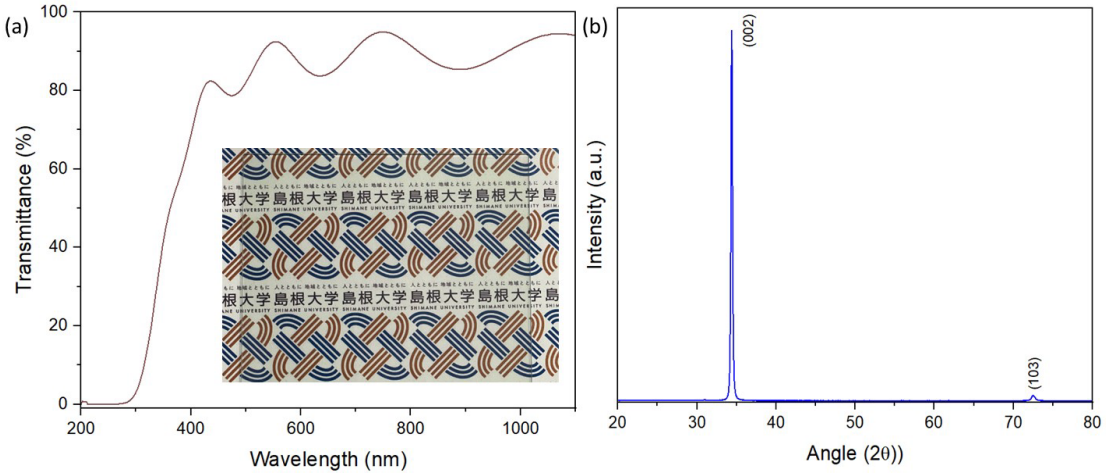

***Figure 16**. **(a)** Transmission spectra of GZO, inset: photo of GZO **(b)** XRD of GZO.*

The thin film thickness was measured using a NanoCalc Spectroscopic Reflectometer and was found to be around 600 μm, and its resistivity was calculated by Hall methods via the Van der Pauw Method equipped with a magnet generating a magnetic field of 1.5 T and was around 9 × 10^{-4} Ω cm, mobility 13.2 cm^2/Vs and electron carrier concentration of $5\times10^{20}/cm^3$.

Ga doping in ZnO films creates either interstitial Ga defects or substitution of Ga^{3+} ions for Zn^{2+} ions in the ZnO lattice or crystal structure. In regard to this substitutional defect, Ga acts as an electron donor that donates to the n-type conductivity of ZnO films. **Figure 16b** shows the XRD pattern of the fabricated GZO film deposited on the glass substrate. The XRD graph shows sharp and intense peaks of the GZO film deposited on the glass substrate obtained at ~34.67°

corresponding to (002) and a slight peak ~72.69° corresponding to (004), which affirms that the GZO films are highly crystalline and oriented with their crystallographic c-axis orientation. The GZO thin films had slightly high 2-theta values when compared to the ZnO powder diffraction angle (34.42°). The presence of Ga^{3+} in the material leads to a reduction in a lattice parameter as the ionic radius of the Ga^{3+} cation (0.062 nm) is smaller than that of the Zn^{2+} cation (0.074 nm), leading to the substitution defects of Ga^{3+} [61].

3.1.2 Spin coating layer formation

The dispersed ZnO NPs were spin-coated over the Ga-doped ZnO (GZO) thin film in order to build the p-type layer.

3.1.2.1 Preparation of dispersion

For the spin-coating layer, the dispersion of ZnO NPs was prepared by mixing 0.1 g of binder (Silsesquioxane OX-SQ SI 20) with 0.05 g of ZnO NPs and 0.3 mL of isopropyl alcohol (IPA). A vortex mixer was used to mix the binder and NPs evenly. The rotation speed of the vortex mixer was set to 3000 rpm, and the time was set to 5 minutes. Initially, the particles are agglomerated and affect the spin coating layer. To remove the agglomeration and make the particles of uniform size using ultrasonic waves, an ultrasonic homogenizer is used. The ultrasonic homogenizer generates pressure waves by vibration to separate and disperse non-uniform particles in the dispersion. The output power was set to 150 W with 3 minutes of the ON cycle and 3 minutes of the OFF cycle. Thereby, ZnO NPs were dispersed to prepare for suspension. After using an ultrasonic homogenizer, it was found that many air bubbles were present with the dispersion, which would not be suitable for the dispersion layer. To remove bubbles generated during suspension preparation, a vacuum-stirring defoaming mixer was used after the ultrasonic homogenizer process.

3.1.2.2 Application of particle layer

The ZnO nanoparticle layer was applied using the spin coating method. Spin coating is a technique that utilizes centrifugal force to evenly distribute a thin film onto a solid surface. Dispersion is placed at the center of a circular surface and is rapidly rotated to produce uniform films. The centrifugal force of the rotation causes the liquid to spread into a film and coat the GZO. A thin dispersion film was formed under the conditions shown in **Table 2** by dropping 50 µl of the suspension onto the GZO base placed on the rotating top. The rotation speed was adjusted in two stages for film thickness uniformity. Later, the spin-coated layer was sintered using a hot plate for 60 seconds at 280 °C. The spin-coated layer had a thickness of approximately 3 µm [62].

Table 2. *Spin coating conditions.*

	Rotational speed [rpm]	Time [s]
1st stage	1000	5
2nd stage	4000	10

3.1.2.3 Electrode deposition

After coating the dispersion layer, a gold electrode is deposited to make the electrical contact for the LED. In this case, also, resistive heating is used to evaporate gold and make contacts. First, undesired reactions are eliminated by evacuating the chamber to low pressure (10^{-3} Pa or less). A resistive DC of 15 A melts the gold. The thin gold film is evaporated over the substrate 1 mm X 1 mm with a mask in high vacuum conditions. For p-and n-type contacts, 30 nm of Au was thermally deposited. The area of the LED was 1 mm^2.

3.2 LED characterization process

A high-resolution SMU module (Keysight Technologies, *B2900A*) was used to characterize the fabricated LEDs. The electrical parameters like voltage and current were measured. An optical fiber was coupled with a spectrometer (Ocean Optics *QE65000* fiber multichannel monochrome meter) and used to characterize the output wavelength of the LEDs. The output EL power of the LEDs was measured by keeping the LED over a Si-based photodetector.

3.2.1 *I-V* curve characterization

At room temperature, the *I–V* characteristics of the LEDs showed a diode-like rectification character with a low threshold voltage of 4.0 V. Au contact with the n-type ZnO and p-type ZnO layers shows good ohmic behavior, as demonstrated in previous work [63].

Figure 17 shows the *I-V* characteristics of p-ZnO/GZO LEDs fabricated using ZnO NPs prepared at a chamber pressure of 150 Torr and with arc currents ranging from 20 to 60 A. Significant leakage current is observed in most of the conditions. This might be due to the effect of the binder; however, it significantly reduces when the LEDs are fabricated with the ZnO NPs obtained under higher current conditions in the discharge chamber.

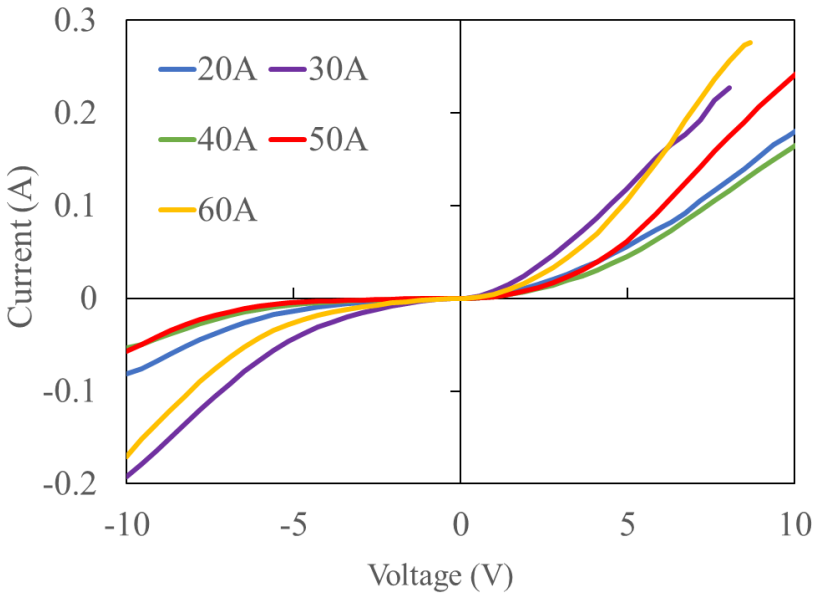

Figure 17. *I-V characteristics of p-ZnO/GZO LEDs fabricated using ZnO NPs prepared at chamber pressure of 150 Torr and with arc currents ranging from 20 to 50 A. (Ref 55)*

3.2.2 Electroluminescence (EL) characterization

Figure 18a shows the electroluminescence characteristics of p-ZnO/GZO LEDs fabricated using ZnO NPs prepared at a chamber pressure of 150 Torr and with arc currents ranging from 20 to 60 A. EL spectra show only UV emissions near the band edge, and defect-related emissions get saturated because more injection current is present in comparison to PL, which was excited by weak-intensity light. Observations indicate that the EL spectra are characterized by a narrow full width at half maximum (FWHM) of 172 meV. This indicates that the emission is caused by the radiative annihilation of excitons [64]. **Figure 18b** represents the schematics of UV-LED. Purple EL emission under a forward bias was observed in a dark atmosphere at ambient temperature. Typically, the ZnO near-band edge (NBE) emission, which arises from the recombination of localized excitons, is accountable for the generation of the UV emission band, peaking at approximately 380 nm.

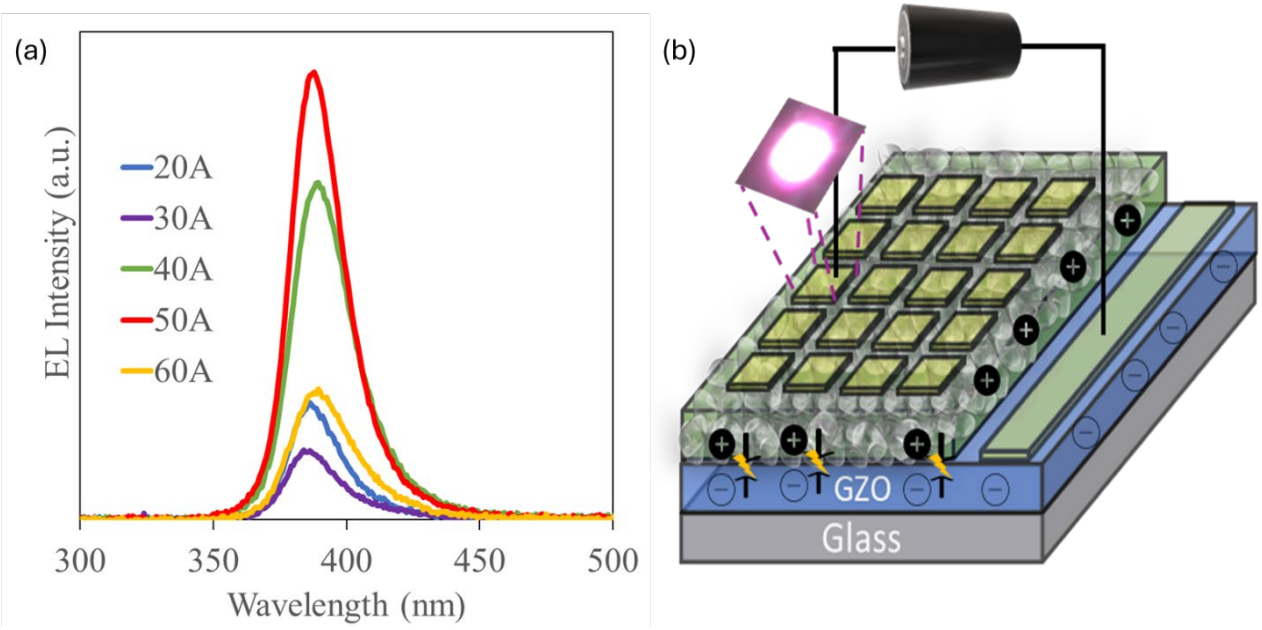

***Figure 18**. **(a)** EL characteristics of p-ZnO/GZO LEDs fabricated using ZnO NPs prepared at chamber pressure of 150 Torr and with arc currents ranging from 20 to 60 A (Ref 55), **(b)** UV-LED schematics. (Ref 67)*

3.2.3 Output power characterization

The LEDs' output powers were determined based on the measured photocurrent generated by a photodiode, taking into account the already-known sensitivity of Si-based photodetectors at given wavelengths. Due to the absorption and reflection at the glass substrate, the measured emission of the LEDs was assumed to be 12 times diminished than the actual emission [62]. **Figure 19** shows the output power of p-ZnO/GZO LEDs fabricated using ZnO NPs prepared at a chamber pressure of 150 Torr and with arc currents ranging from 20 to 60 A. A schematic representation of the measuring setup is shown in the figure inset. The output power of LEDs formed with ZnO NPs fabricated with a chamber pressure of 150 Torr and an arc current of 50 A showed maximum output when compared to other fabrication conditions.

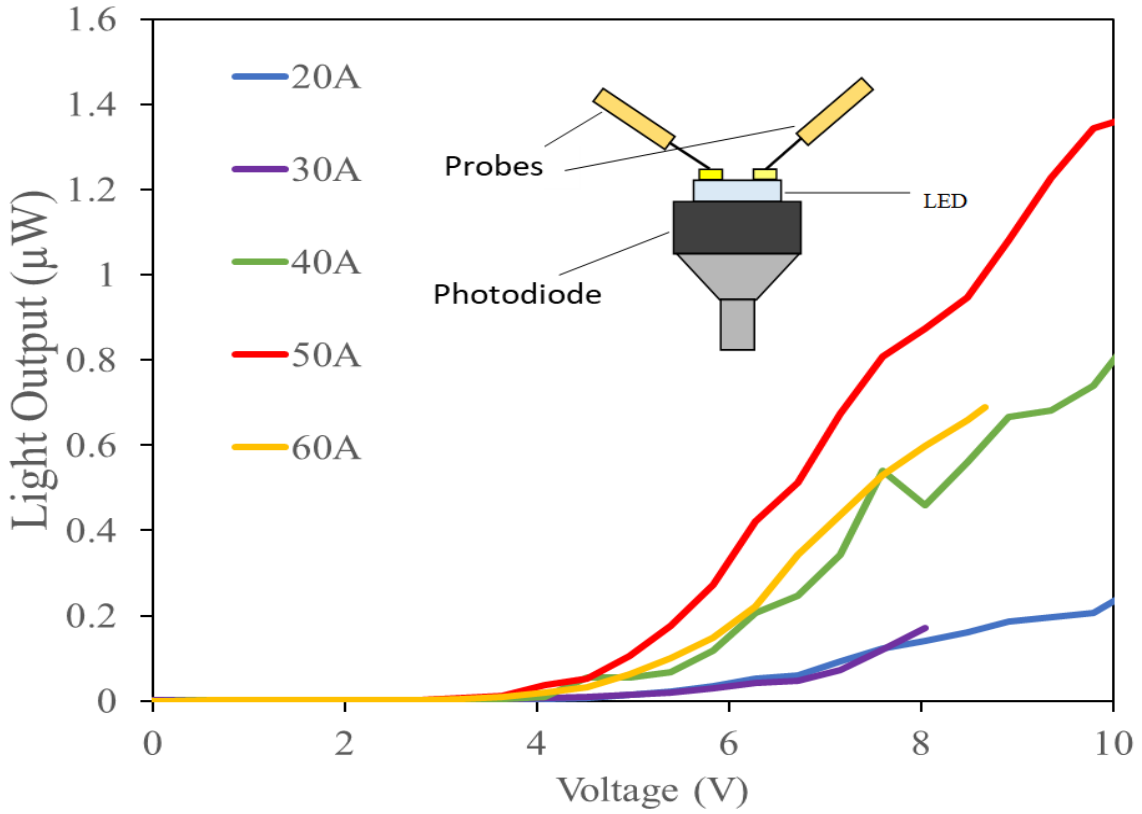

***Figure 19**. Output power of p-ZnO/GZO LEDs fabricated using ZnO NPs prepared at a chamber pressure of 150 Torr and with arc currents ranging from 20 to 60 A. (Ref 55)*

The effect of the nitrogen concentration variation is studied fabricating the device. **Figure 20** shows the comparison of the EL results of the LED with the ratio of the DAP/exciton emissions observed from the PL results. In the figure, a linear relationship can be observed for both the DAP/exciton emissions and the EL intensity. Therefore, the presence of nitrogen in ZnO NPs directly influences the DAP luminescence and the performance of the device.

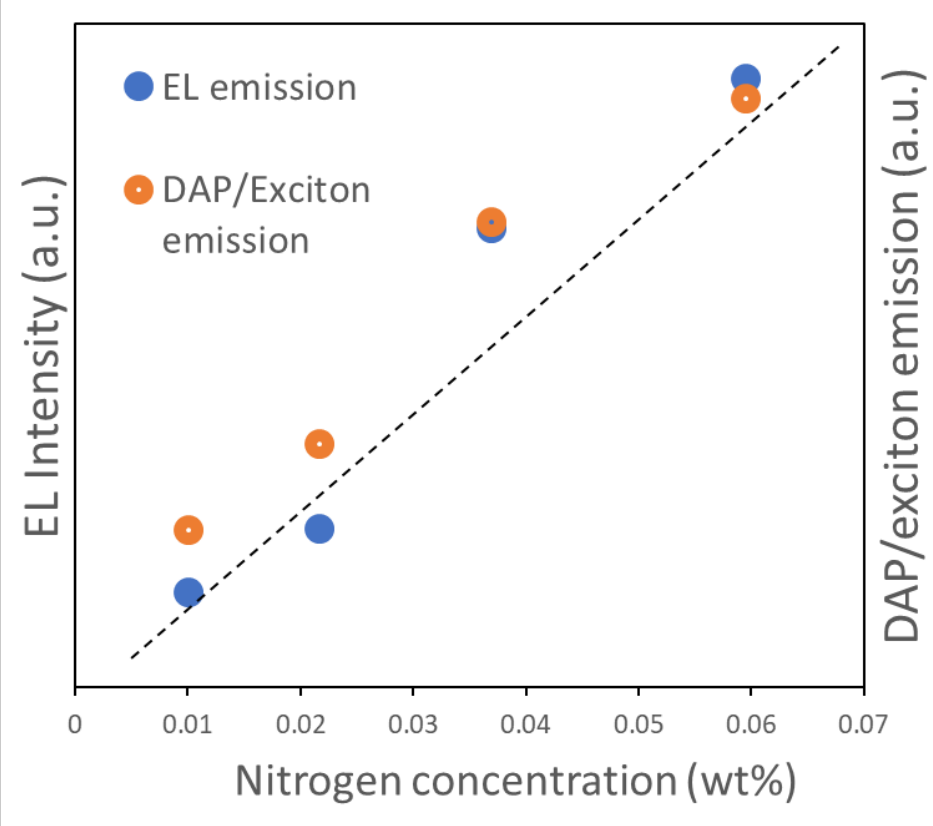

Figure 20. *Ratio of DAP/exciton emissions and EL intensities with variable nitrogen concentration. (Ref 55)*

3.3 Conclusion

In this chapter, the fabrication and characterization of ZnO NP-based LEDs are discussed. A Spin-coating p-type layer is employed on the glass-based GZO. The device is characterized by *I-V*, EL, and output power. At low plasma temperatures, the incorporation of the nitrogen dopants is favorable, and they act as acceptors in the ZnO NPs, which is further confirmed by the fabrication of nanoparticle-based LEDs.

Major research findings of chapters 2 and 3 have been published (Deep, R., Akazawa, T., Yoshida, T., & Fujita, Y. (2023), "A Spectroscopic Evaluation of the Generation Process of Semiconductor Nanoparticles (ZnO) by DC Arc Plasma", J, 6(2), 207-219).

Chapter 4. Role of defects

4.1 Introduction

ZnO represents a very versatile semiconductor material, applied in the areas of electronics, optoelectronics, and catalysis. Similar to all other materials, ZnO can have defects that might alter or affect its properties. The representation of an ideal defect-free ZnO is shown in **Figure 21 a**.

The intrinsic factors could be due to thermal vacancies, and the extrinsic factors include impurities like doping or parameters pertaining to the environment. Some of the point defects are mentioned as follows:

Vacancies: Vacancies are created when an atom is missing from its lattice site. Zinc vacancies (V_{Zn}), and oxygen vacancies (V_O), have been commonly reported in ZnO. These vacancies often change the electronic and optical parameters of ZnO.

Interstitials: Interstitial defects occur when extra atoms are located at positions in a lattice normally occupied by empty space. For ZnO, interstitials can be zinc interstitials (Zn_i) or oxygen interstitials (O_i). These further impact the conductivity and optical properties of ZnO.

Substitutional defects: Substitutional impurities occur due to the replacement of the original atoms in the lattice by atoms of other elements. For example, in ZnO, aluminum (Al), gallium (Ga) and indium (In) substitute for zinc, leading to n-type doping. Similarly, nitrogen (N) and phosphorus (P) replace oxygen (O) and yield p-type doping.

Typically, intrinsic ZnO exhibits n-type conductivity due to the inherent defects, mostly zinc interstitial (Zn_i), zinc antisite (Zn_O), oxygen vacancy (V_O), and/or hydrogen incorporation. In ZnO, intrinsic donors' self-compensation effect prevents p-type doping. Obtaining p-type doping in ZnO has proven to be difficult and rarely accomplished due to the low solubility of acceptor dopants

and deep acceptor energy level. Zinc vacancy (V_{Zn}), oxygen antisite (O_{Zn}) and oxygen interstitial (O_i) act as acceptor defects among the native defects in undoped ZnO.

We have used nitrogen as the dopant to make p-ZnO. Some of the intrinsic and extrinsic defects in the ZnO are shown in **Figure 21b**.

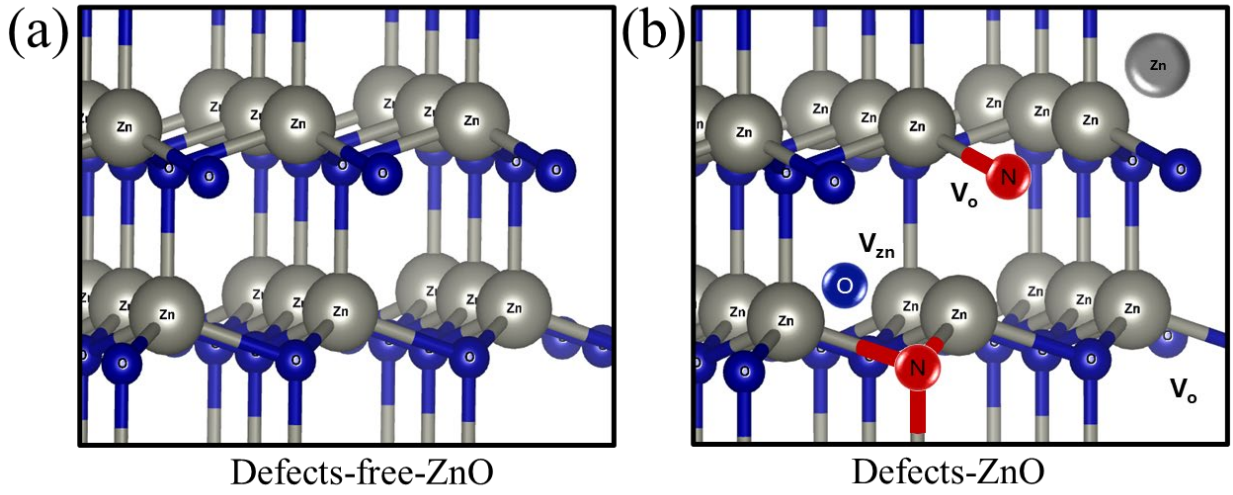

***Figure 21. (a)** Defect-free-ZnO **(b)** defects-ZnO as simulated by VESTA software.*

Furthermore, it is widely acknowledged that the level of defects in ZnO NPs has a substantial influence on their physical attributes and optoelectronic properties. The concentration of defects can be modified and controlled by adjusting the annealing conditions [65]. Typically, the material that is in its original state is likely to have H-N complexes. The process of annealing can assist in separating these complexes, thus making the N acceptors "active". Experimental findings indicate that after high-temperature annealing, most of the hydrogen-related local vibrational modes (LVMs) and multiphonon modes were absent [66]. Due to the impact of defects on the p-type characteristics of ZnO NPs, LEDs were fabricated and evaluated to see how they are impacted by the defects [67].

4.2 Experimental procedures

Effects of heat on NPs were studied by annealing the as-prepared ZnO NPs in the annealing furnace. The schematic diagram of the annealing equipment is shown in **Figure 22**. In this experiment, two types of ambient gas were used for annealing: one was pure O_2 with a purity of 99.9 %, and the other was pure N_2 with a purity of 99.99 % was used to anneal the as-prepared samples. A vacuum pump was used to remove the air from the chamber after the ZnO NPs were inserted, and pure gases were flushed out to eliminate any impurities. A continuous gas flow of 0.5 L/min is provided to the chamber throughout the process. In all fabrication processes, the temperature of the furnace was elevated from the initial room temperature to 800 °C within a span of 10 minutes. Following a 60-minute thermal treatment, the samples were gradually cooled down to room temperature within 2 hours. After annealing, ZnO NPs seem to clump together and the color of the as-prepared changes to white from pale pinkish-white. This might be due to the result of rapid annealing of ZnO NPs.

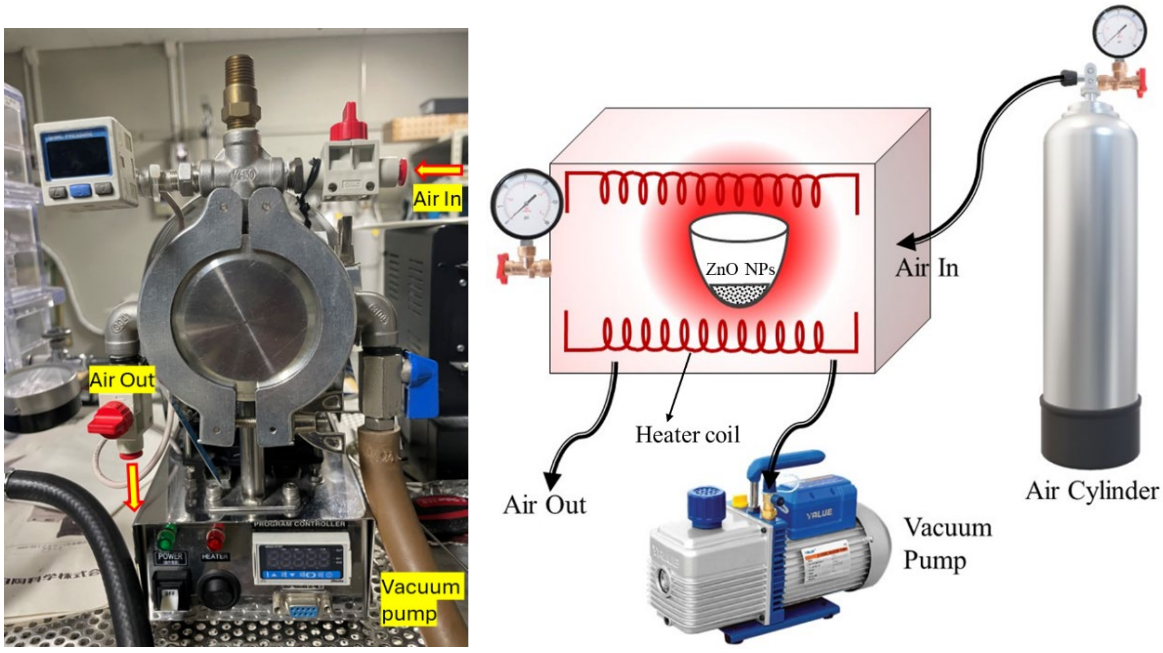

***Figure 22**. Schematic diagram of annealing equipment.*

4.3 X-ray diffraction (XRD)

XRD is among the general techniques used in the analysis of ZnO NPs to identify their crystal structure and composition of phases. Normally, ZnO NPs manifest a wurtzite crystal structure, which can be confirmed by XRD besides other size and strain information of the NPs. The structure of the synthesized NPs was examined using a Rigaku Smart Lab X-ray diffractometer. The diffractometer utilized *CuKα* radiation at 40 kV and 50 mA, with a scanning speed of 5°/min and a step width of 0.002°. The scanning range for the analysis was set from 20 to 80°.

The highly crystalline nature of the as-prepared ZnO and annealed NPs was confirmed by the XRD results. The crystal structure was wurtzite in nature. It was found to agree with the diffraction peaks reported in the JCPDS with card number 36-1451. There is no extra diffraction peak corresponding to other different phases, thus indicating that ZnO NPs synthesized by the plasma arc discharge method have high-quality crystallization. The alignment of the crystallites was preferred along the (100), (002), and (101) planes in as-prepared ZnO NPs and annealed ZnO NPs. After annealing the samples at 800 °C in an O_2 and N_2 ambient, the overall diffraction pattern remains similar, as shown in **Figure 23a**. When ZnO NPs annealed in the N_2 ambient, the peaks shifted to higher angles, whereas in the O_2 environment, the broadening of diffraction peaks was observed with a reduction in peak intensity, as shown in **Figure 23b** represents the XRD peak of the (002) plane. Both the size of the crystallite and the microstructure of the lattice have an impact on the broadening of diffraction peaks. However, a detailed analysis of the XRD data reveals the distinct variations in the structure of annealed particles, such as the size of the crystallites, the density of dislocations, and the presence of microstrain.

The size of the crystals in the samples was estimated from diffraction intensities at the (100), (002), and (101) planes using the Debye-Scherrer equation. While annealing in an O_2 environment

decreased the average crystallite size to 46 nm, annealing in an N_2 environment increased it to 61 nm, as shown in **Figure 24**.

Crystallite size can be measured by $D = \frac{0.9\lambda}{\beta \cos\theta}$ where λ is the wavelength of the radiation, θ is the Bragg angle and β is the full width at half maximum of the diffraction peaks. The estimate of the size of crystallites also allows for the evaluation of the structural integrity of the polycrystalline NPs by calculating the parameter $\delta = (1/D^2)$, which is linked to the density of dislocations. The δ parameter allows for a qualitative evaluation of structural flaws, such as grain boundaries, that affect the crystallographic integrity of NPs [68]. In the O_2 ambient, the average dislocation density of ZnO NPs increased, while in the N_2 ambient, it was less as compared to the as-prepared samples. The lower value of δ signifies that the NPs that underwent annealing in a nitrogen ambient possess a minimal amount of lattice defects and demonstrate superior crystalline characteristics in comparison to the samples that were annealed in an oxygen ambient.

Microstrain (η) is estimated using the relation, $\eta = \frac{\beta}{4\tan\theta}$, As can be seen from **Figure 24**, the microstrain in the ZnO NPs when annealed in the N_2 ambient is similar to as-prepared NPs. The comparison of microstrain between as-grown ZnO NPs and those annealed under the N_2/O_2 atmosphere reveals that annealed ZnO in the O_2 atmosphere experiences increased microstrain in comparison with as-prepared ones following the dislocation density.

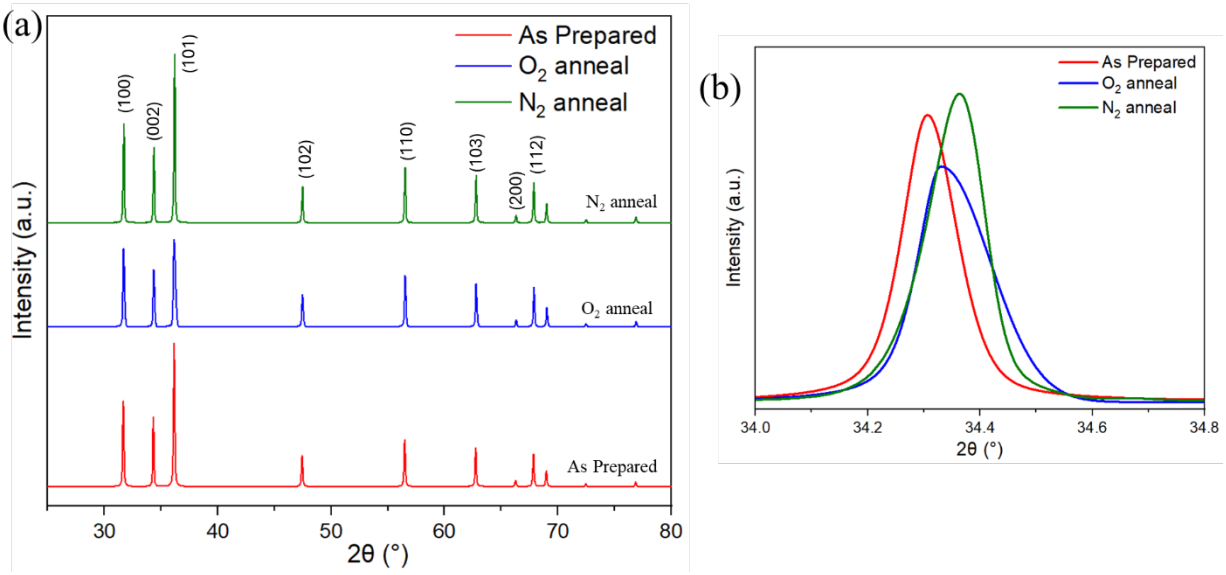

***Figure 23**. **(a)** X-ray diffraction pattern of as-prepared and annealed ZnO NPs, **(b)** XRD peak of the (002) plane. (Ref 67)*

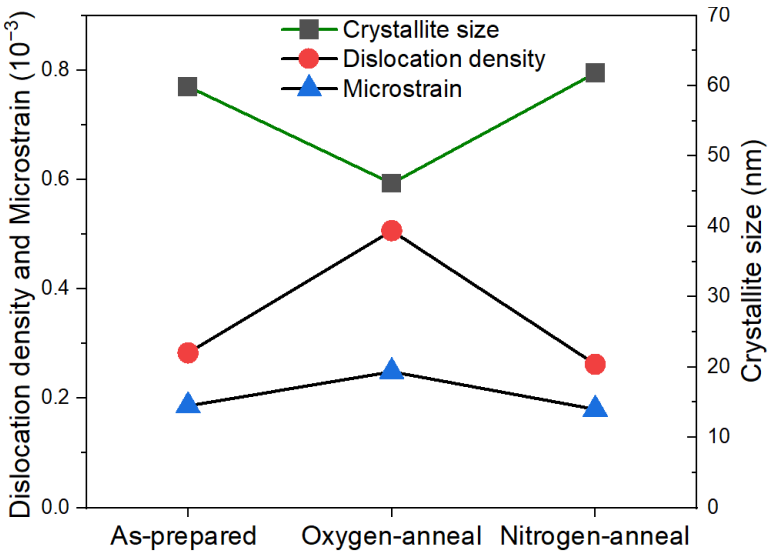

***Figure 24.** Relation between dislocation density, microstrain and crystallite size. (Ref 67)*

The lattice constants are calculated within the hexagonal lattice parameters, wherein d_{hkl} is the interplanar spacing of (*hkl*) planes, determined from Bragg's law, $2d_{hkl}\sin\theta = n\lambda$. **Table 3** depicts the lattice constants for ZnO in the hexagonal closed packing (hcp) orientation which are calculated using the equation that relates them to the lattice parameters.

$$\frac{1}{d^2} = \frac{4}{3}\left(\frac{h^2+hk+k^2}{a^2}\right) + \frac{l^2}{c^2}$$

Table 3. *ZnO lattice constants (measured from XRD).*

Samples	**Lattice constants (Å)**		**Lattice Distortion (%)**
	a	**c**	
As-prepared	3.256	5.217	0.039
N_2-anneal	3.253	5.211	0.044
O_2-anneal	3.252	5.209	0.038

Lattice distortion tends to increase after annealing under the N_2/O_2 atmosphere.

4.4 Scanning Electron Microscope (SEM)

The size, shape, and morphology of the annealed NPs and as-prepared ZnO were studied using a field-emission scanning electron microscope (FE-SEM) operated at 5 kV. **Figure 25** displays the scanning electron microscope (SEM) images of ZnO NPs before and after annealing in an N_2/O_2 atmosphere. Under non-equilibrium conditions, the plasma undergoes scattering and cooling, leading to the interaction of its components and the formation of clusters and NPs. A combination of NPs, nanorods, tripods and tetrapods, displaying a well-defined crystal structure is seen in the ZnO NPs, as-prepared and N_2-annealed ones. However, the crystal structure of O_2-annealed ZnO NPs has the aspect ratio, leading to low crystalline qualities, likely because of the higher micro-strain or dislocation density.

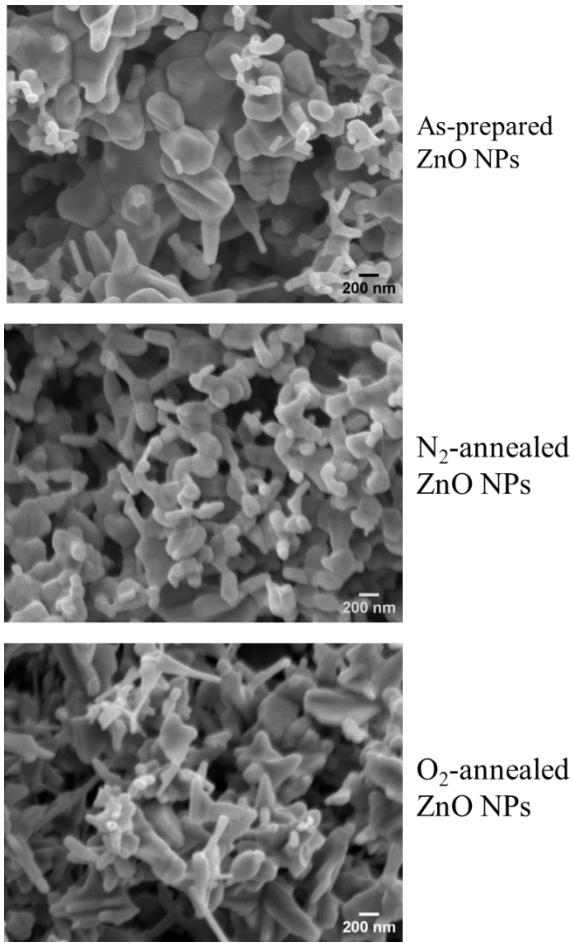

Figure 25. *SEM images of as-prepared and annealed ZnO NPs. (Ref 67)*

4.5 Raman spectroscopy

Raman spectroscopy provides information about structural, optical, and electronic properties. That said, Raman scattering has been used in this present study to probe the vibrational modes of nitrogen-doped ZnO NPs. Wurtzite ZnO belongs to the C_{6v} symmetry group, with Raman-active phonon modes E_2 (low), E_2 (high), A_1 (TO), A_1 (LO), E_1 (TO), and E_1 (LO) observed at 100, 438, 380, 574, 409, and 584 cm^{-1}, respectively. In addition to intrinsic modes, nitrogen-related local vibrational modes (LVMs) were observed in the samples. Additionally, LVMs were detected using Raman spectroscopy at 275, 510, and 580 cm^{-1} in the prepared sample. Kaschner et al. also observed Raman peaks in the ZnO film doped with nitrogen at 275 and 580 cm^{-1}, similar to the results previously reported [69]. The presence of nitrogen-related impurities was hence expected

within ZnO NPs, which was evidenced through optical signatures of atomic and molecular nitrogen transitions during the synthesis of ZnO NPs at lower chamber pressures. The underlying reason behind the acceptance of ZnO can be attributed to the existence of nitrogen.

The as-prepared ZnO NPs and annealed ZnO NPs were studied using a confocal micro-Raman spectrometer in order to examine the impact of annealing on the nitrogen content in ZnO. The fabricated ZnO has a hexagonal wurtzite structure in relation to the $P6_3mc$ space group. **Figure 26** shows the Raman spectra of the as-prepared and annealed ZnO NPs in N_2 and O_2 environments. The intense Raman active, non-polar phonon mode at 438 cm^{-1} (E_2(high)), which is characteristic of the hexagonal wurtzite crystal structure is observed in all samples. Other polar phonon modes like A_1 (TO) and E_1 (LO) optical modes appeared at 380 cm^{-1} and 584 cm^{-1}, respectively. In addition to the inherent modes, certain nitrogen-related local vibrational modes (LVMs) were also detected in the Raman spectra at 275 cm^{-1} and 580 cm^{-1} in as-prepared samples. The presence of nitrogen-related LVMs confirmed the acceptor properties of p-ZnO NPs. These peaks were considerably reduced after annealing of the samples in an O_2 atmosphere, while they remained quite strong for N_2-annealed samples.

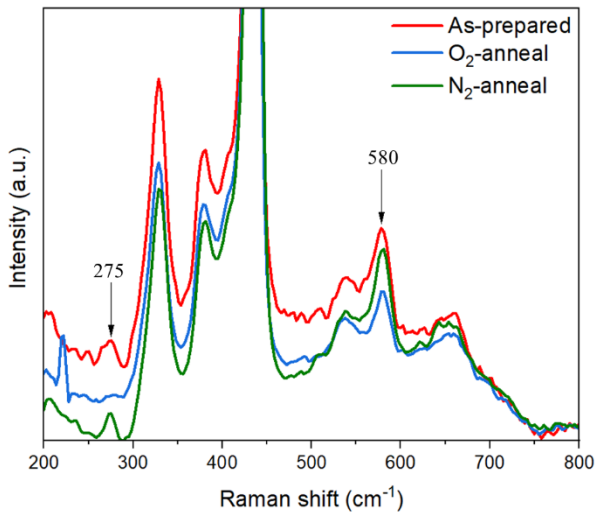

Figure 26. *Raman spectra of as-prepared and annealed ZnO NPs. (Ref 67)*

4.6 Photoluminescence

The optical properties of as-prepared ZnO NPs were measured by the photoluminescence spectrum at room temperature, as shown in **Figure 27**. In this setup, PL was excited by weak-intensity UV light (Xenon light source). Most of the photoluminescence spectra reveal two clearly defined peaks: one narrow in the near-ultraviolet range, approximately at 380 nm, and another wider peak of emission in the visible range from deep levels between 450 and 600 nm. The UV intensity peak seems to be suppressed after annealing, while a slight redshift is observed in the visible region for the annealed samples. Post-annealing generally leads to a decrease in the intensity of near-band-edge (NBE) emissions as an influence of dopants. The reduction in NBE can be ascribed to alterations in the inherent defects, such as Zn_i, V_O, and V_{Zn}. In order to investigate the impact of an annealing environment on the PL characteristics of ZnO NPs, the PL spectra are deconvoluted into four major distinct peaks using Gaussian functions: the UV emission at 383 (±3) nm, Zn_i at 473 (±3) nm, V_o at 497 (±3) nm, and V_{zn} at 523 (±3) nm respectively [70]. The deconvoluted photoluminescence spectra for as-prepared ZnO NPs are shown in **Figure 28a,** O_2-annealed ZnO NPs are shown in **Figure 28b,** and N_2-annealed ZnO NPs are shown in **Figure 28c**. In the case N_2 annealed samples, V_{zn} was dominant, indicating better acceptor properties, while in the O_2-annealed samples, there was an increase in oxygen-related vacancies, which are responsible for donor-related properties. Annealing resulted in the increase of V_O in an oxygen environment while being suppressed in a nitrogen environment. This increase in V_O might be due to the out-diffusion of nitrogen. Annealing will decrease it to approximately one-tenth of its original value. Thermal conductivity methods were employed to measure the nitrogen content. The nitrogen concentration was close to 10^{18}~10^{19} cm^{-3}. This concentration also includes surface adsorption of nitrogen, so actual nitrogen displacing oxygen sites will be slightly different.

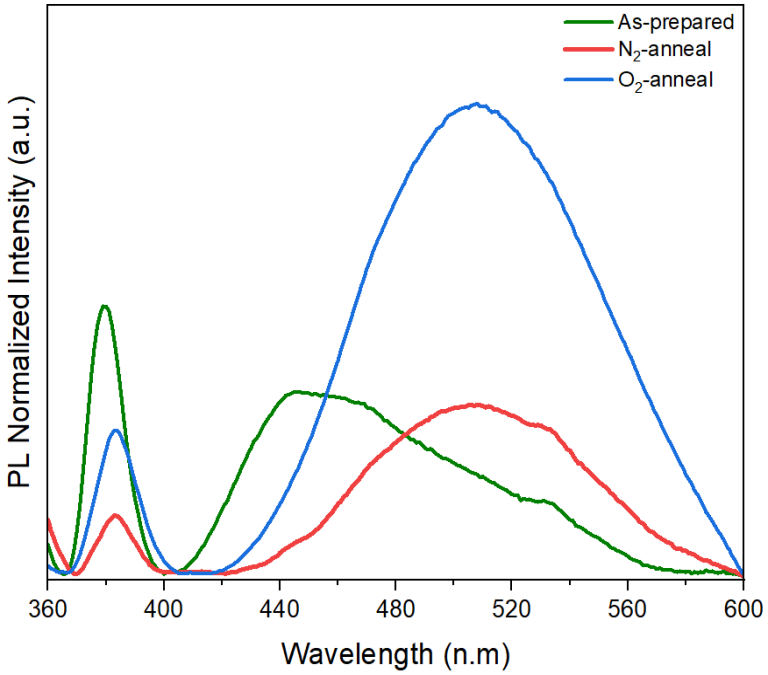

Figure 27. *PL spectrum of as-prepared and annealed ZnO NPs. (Ref 67)*

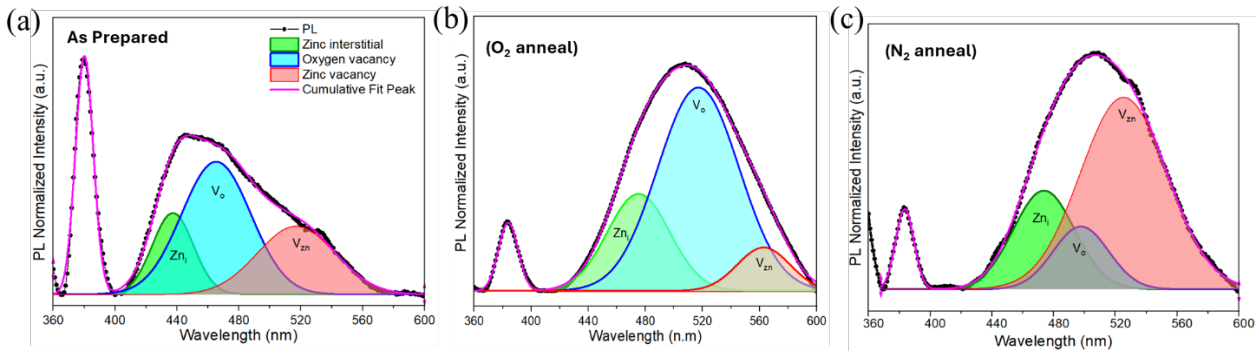

Figure 28*. **(a-c)** Deconvoluted PL spectrum of as-prepared and annealed ZnO NPs. (Ref 67)*

Meanwhile, the output power of annealed and as-prepared ZnO NP-based LEDs was compared and correlated with the luminescence caused by defects, as shown in **Figure 29**. In the case of O_2-annealed ZnO samples, oxygen vacancy-related defects were prevalent in the sample and thereby the output power of the LEDs was low when compared with as-prepared samples. Degradation in acceptor-like properties in ZnO NPs was observed, probably due to the increase in oxygen deficiency and the presence of relatively less nitrogen, which acts as an acceptor dopant. Thus, V_o can be credited to enhance the n-type conductivity in ZnO, which was both theoretically predicted

and experimentally verified, whereas the output power of the LEDs in the case of nitrogen-annealed samples increased, as V_{zn}-related defects were dominant, leading to better results. The enhanced power output of LEDs can be ascribed to the efficient radiative recombination of excitons, which could be the result of an increase in acceptor-related defects. Therefore, a lack of zinc could potentially reduce the energy needed for the acceptor level. Similar findings have been experimentally verified by Chavillon *et. al.* using transient and electrochemical spectroscopy and concluded that the stability of p-type conductivity was due to Zn-deficient NPs [71].

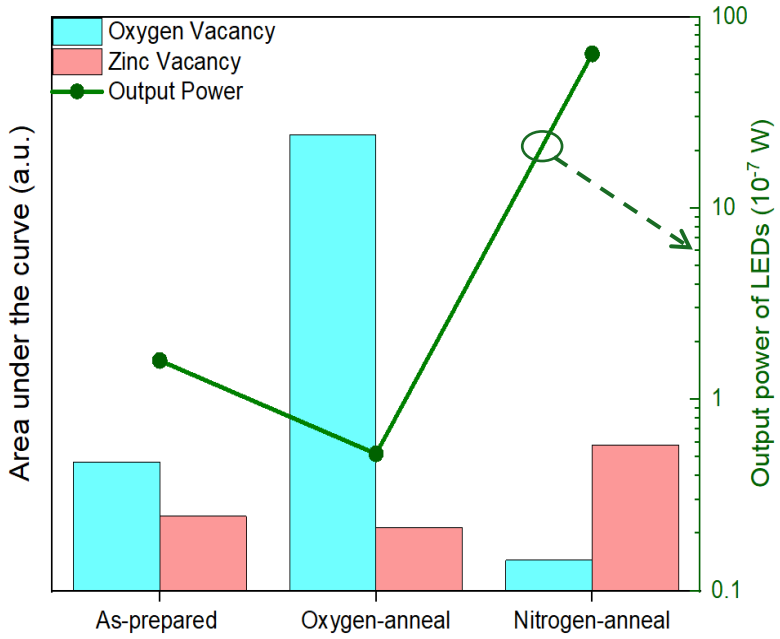

Figure 29. *Relation between defect luminescence and output power of LEDs. (Ref 67)*

4.7 Photoluminescence Quantum Yield (PLQY)

The photoluminescence quantum yield is a measure of the effectiveness of light emission following material absorption of photons. It is the ratio of the number of emitted and absorbed photons by the material. High PLQY is required in applications such as LEDs. That means it shows how the material converts absorbed photons into emitted photons. The PLQY of the prepared and annealed ZnO NPs was measured by using a Horiba F-3018 integrating sphere within a

FluoroMax-4 spectrofluorometer. The PLQY of the samples, as prepared, was about 3.5%. It increased to about 4.6% for nitrogen-annealed samples and decreased to about 3% for oxygen-annealed samples. For ZnO NPs, the increase in PLQY results from an increase in the carrier density. Therefore, because of this, there is an increase in the rate of activation of the acceptors, hence improving EL.

4.8 Conclusion

These studies now clearly reveal that the main determining factor for p-type behavior demonstrated by ZnO is the combined effect of acceptor doping and Zn deficiency in nitrogen-doped ZnO nanoparticles. This prediction is theoretically calculated and has been supported by experiment data including photoluminescence, Raman spectroscopy, and LED formation. It was deduced from the results of the experiments that the zinc vacancies in nitrogen-doped ZnO behave as acceptors, further enhancing the p-type nature of ZnO. Oxygen vacancies, however, are electron donors and hence deteriorate the performance of the developed LED devices. Finally, this is the first experimental evidence that zinc vacancies enhance the p-type properties of nitrogen-doped ZnO NPs. These findings are a significant advancement in identifying the main inherent and external defects that impact the acceptor-like properties of nitrogen-doped ZnO NPs.

Major research findings of chapter 4 have been published (Deep, R., Yoshida, T., & Fujita, Y. (2024), “Defects in Nitrogen-Doped ZnO Nanoparticles and Their Effect on Light-Emitting Diodes”. Nanomaterials, 14(11), 977).

Chapter 5. Visible light from ZnO NPs LEDs using phosphors

5.1 Introduction

Phosphor-converted LEDs (pc-LEDs) are considered feasible substitutes for conventional LED systems among the different types of light-emitting diodes. pc-LEDs offer several benefits compared to conventional lighting sources, such as superior luminous efficiency, minimal power usage, long-lasting durability, eco-friendliness, and an extended operational lifespan. Usually, they are created by applying a layer of phosphors to either the chip itself or the encapsulant resin. The phosphors are transformed into lower-energy light by the ultraviolet (UV) or blue light emitted by the chip [72]. UV-LEDs exhibit better optical stability compared to white light LEDs based on UV or blue light. This is because the changes in optical parameters are minimal, and the variations in the UV regions have less impact than those in the blue regions when adjusting the driving current for calculating optical parameters [22].

5.2 Device fabrication

The schematic diagram is shown in **Figure 30**. ZnO NP-based LEDs were fabricated on aluminum substrate. The GZO deposited on aluminum substrate shows similar properties to the GZO deposited on a glass substrate, as discussed in Chapter 3. The GZO resistivity was around $3.7 \times 10^{-4}\ \Omega$ cm, mobility 16.2 cm^2/Vs, and electron carrier concentration of $1.07\times10^{21}/cm^3$.

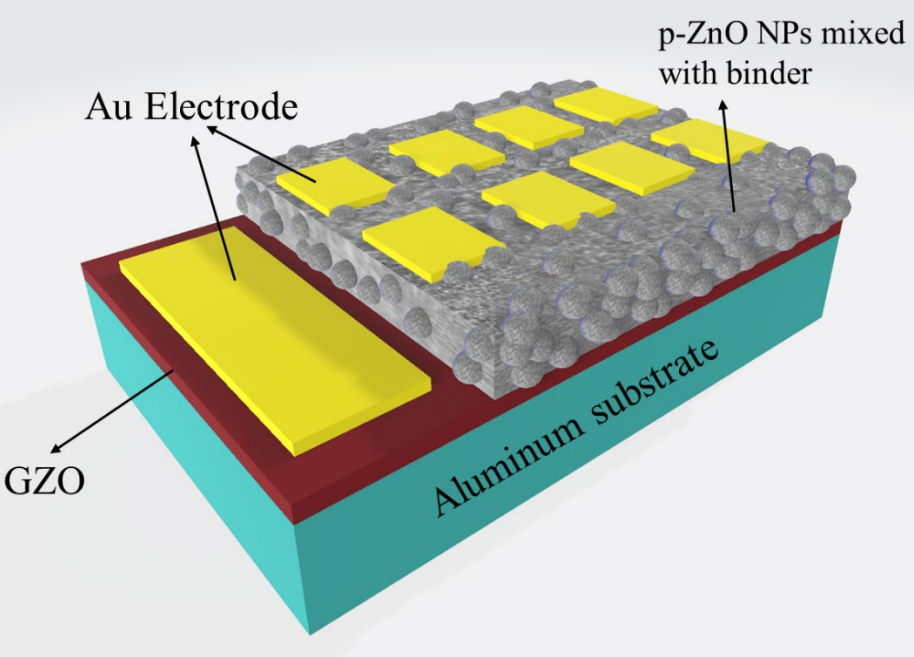

Figure 30. *Schematic diagram of ZnO NPs-based LED.*

The *I-V* characteristic is shown in **Figure 31** fabricated with sodium silicate (Na_2SiO_3) as the binder mixed with ZnO NPs obtained at 50 A. Most LEDs exhibited a high leakage current; however, it was significantly improved when the LEDs were fabricated with sodium silicate (Na_2SiO_3) as the binder, which may be attributed to the passivation of defects [73].

At room temperature, the *I-V* characteristics exhibited diode-like rectification with a turn-on voltage of approximately 3.4 V, which aligned well with the ZnO bandgap energy of 3.37 eV. The rectification ratio was approximately 1600 when the forward and reverse voltages of ±4 V were applied. The *I-V* profile deviated from the exponential relationship over an applied voltage of 4 V owing to the high series resistance of the spin-coated p-type layer.

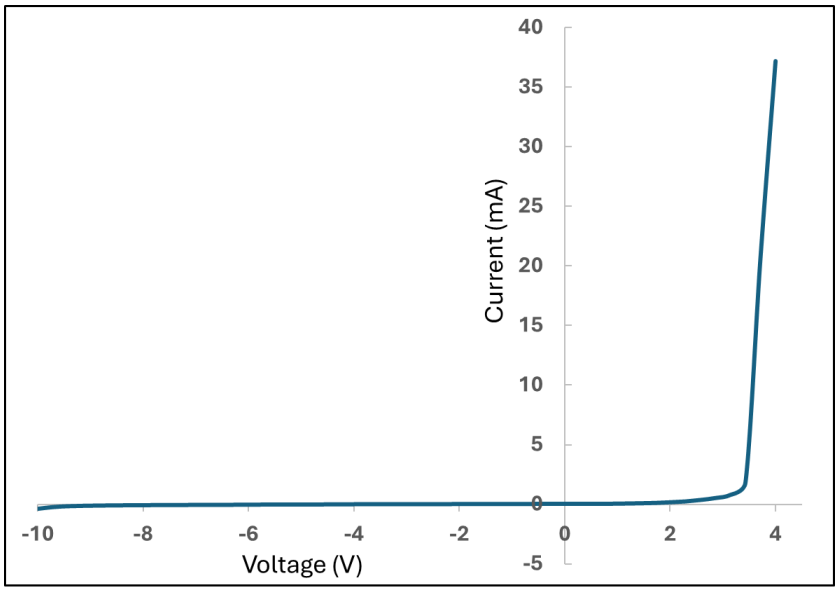

***Figure 31**. I-V characteristic of the LEDs fabricated using water glass as the binder.*

To test the lifetime of the LEDs, the LEDs were subjected to a constant 12 V for 1 hour. In the case of aluminum substrate, the output of the LED was observed from the top side, as shown in **Figure 32**, inset. Thus, the actual output power should be much higher than observed, as very few lights were falling on the photodiodes. The output current reduced from 60 mA to 30 mA in 1 hour, maintaining a constant current for an initial 10 minutes, while a 50% reduction in output power was observed in 1 hour, as shown in **Figure 32**. The performance exhibited by the aluminum-based LEDs was far greater than the glassed ones since they have thermal dissipation. Aluminum has better thermal conductivity, 237 W/mK, compared to glass.

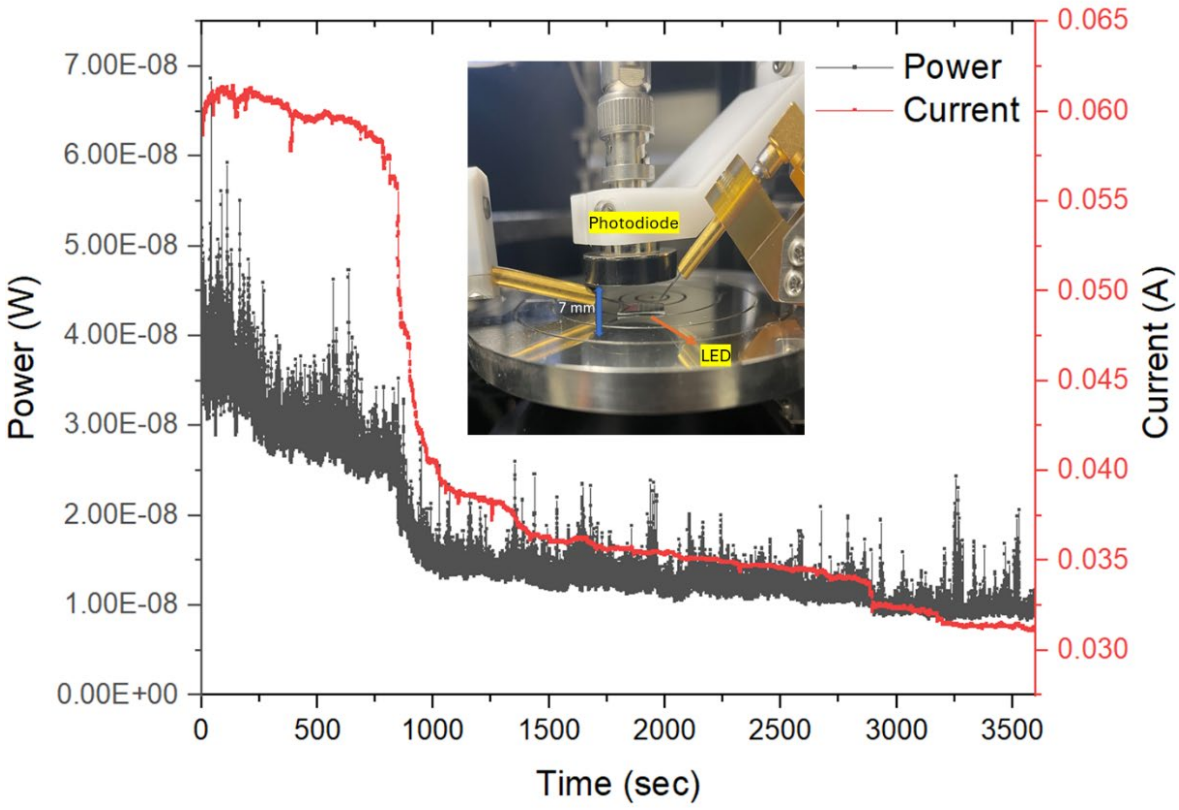

Figure 32. *Lifetime measurement of LED.*

5.3 Heating Effect

The capability of high-temperature performance in ZnO LEDs is important for operation under harsh environments [50]. The high temperatures cause a decay of the exciton state and donor-acceptor pair emission, which may lead to a reduction in the EL intensity. The effect of heating on the EL was studied by varying current injections. As the injection current increased to 20 mA, the EL intensity gradually increased, and a further red shift was observed when the current was increased to 25 mA, emitting maximum luminescence and reaching a peak value. However, when the injection current is further increased, the luminescence exhibits a reduction in the EL intensity owing to heating effects, as shown in **Figure 33a-d**. The corresponding electroluminescence (EL) spectrum for the current injection is shown in **Figure 34**. The redshift may be attributed to the change in the carrier concentration caused by varying the injection current or thermally induced

bandgap narrowing. In addition, high temperatures cause a decay of the exciton state and donor-acceptor pair emission, which may lead to a reduction in the EL intensity. **Figure 35a** shows the photograph of the EL measurement with the Peltier module, while **Figure 35b** shows the emission spectra of the aluminum substrate LED by varying the temperature controlled by the Peltier module in both cooling and heating cycles. A Peltier module was used to heat/cool the LED's surface by varying the voltage's polarity from the DC generator. During the cooling cycle, the Peltier module was helped by the heat sink and fan to extract the heat generated, thereby efficiently cooling the other side. A thermal camera (G120EX Thermo Gear) was used to study the surface temperature of the Peltier module.

A reduction in EL intensity was observed as the surface temperature increased, which was also maintained under continuous operation for a few minutes. It has been reported that the luminous efficacy or optical power decreases with increasing junction temperature owing to the thermal activation of nonradiative Augur recombination or electron-hole recombination. The high thermal conductivity of aluminum enables rapid and uniform heat distribution when the LED is forward-biased, as shown by the thermal image of the LED in the inset of **Figure 35**; this also enables higher injection currents compared to glass-substrate LEDs.

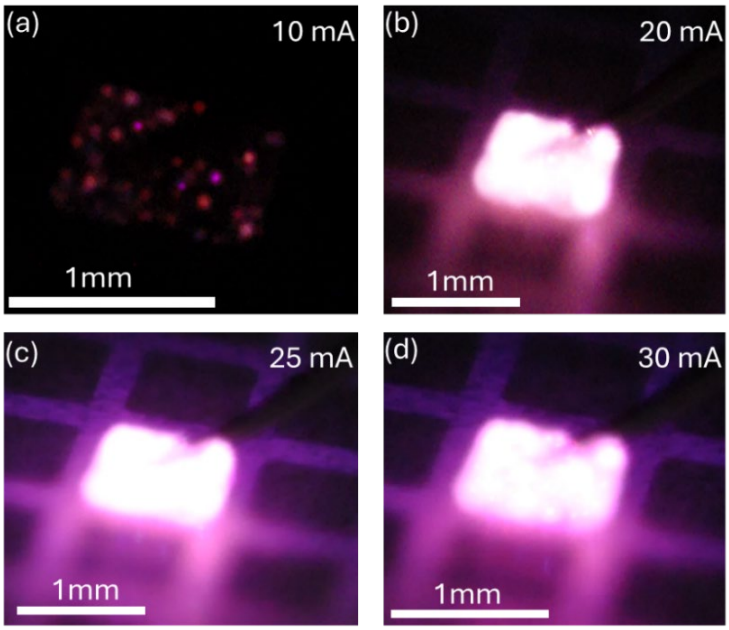

Figure 33. (a–d) *Photograph of UV emission with varying injection current. (Ref 73)*

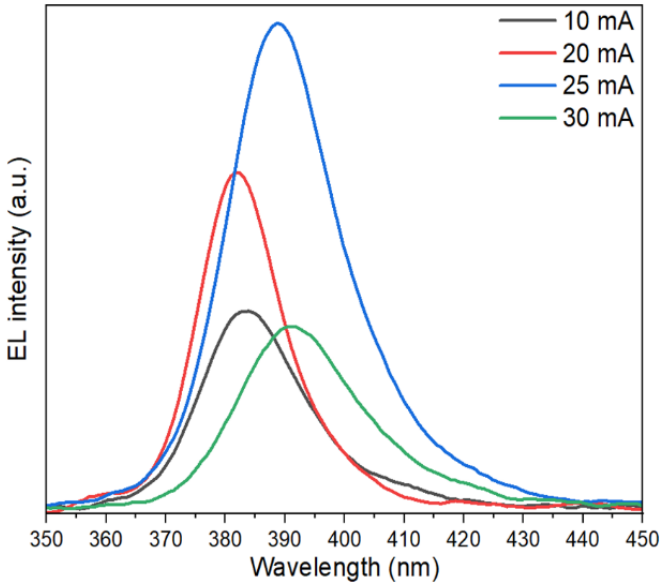

Figure 34. *EL emissions by varying injection current based on aluminum substrate. (Ref 73)*

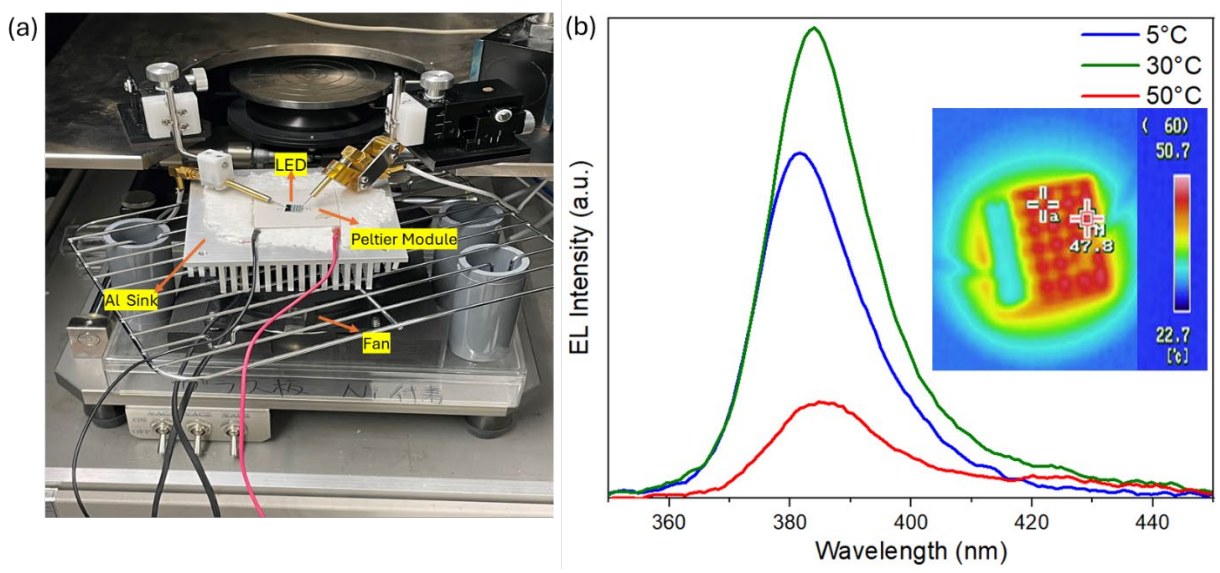

***Figure 35**. **(a)** Photograph of EL measurement with Peltier module, **(b)** EL intensity based on aluminum substrate with variable temperature, inset: the thermal image of the LED during the heating cycle. (Ref 73)*

5.4 Visible LEDs using phosphors

A phosphor layer was prepared to convert the near-ultraviolet emission of a ZnO nanoparticle-coated LED into visible light emission. The phosphors (purchased from Mitsubishi Chemical Corporation), CASN($CaAlSiN_3:Eu_2^+$) phosphor as a red phosphor, β-SiAlON($(Si,Al)_3(O,N)_4:Eu_2^+$) phosphor as a green phosphor, and SBCA($(Sr,Ba)_{10}(PO4)_6Cl_2:Eu_2^+$) as a blue phosphor were used. The phosphor layer formed on the LED was formed by mixing these phosphor particles with an ultraviolet-curable resin (KER-4000), dropping them on an electrode, and curing the resin by UV irradiation with a metal halide lamp. Lamp output power is controlled to 1500W for 3 minutes for proper curing. For making white phosphor, red, green, and blue phosphors were mixed with KER-4000 transparent resin in an equal ratio.

5.4.1 Primary color (Red, Green, Blue) LEDs

For visible emission, phosphors were used over LEDs. Initially, the LEDs were connected in parallel using gold wire and silver paste, with a conductivity of 10 μΩcm, by a manual epoxy die bonder. **Figure 36** shows a schematic diagram of the parallel connection of the two LEDs. **Figure**

37a-c shows an image of the LEDs connected in parallel with the gold wire (diameter: 0.005 mm). Green phosphor β-SiAlON($(Si,Al)_3(O,N)_4:Eu_2^+$) was used to absorb the UV light and emit in green regions. The phosphor was coated over one of the LEDs for the demonstration. The phosphor was mixed with a UV-curable resin and cured using a high-power UV lamp. The green emission is plotted in the Commission Internationale de l'Eclairage (CIE) 1931 XY chromaticity diagram in **Figure 37d**, where (0.33, 0.61) are the X and Y chromaticity coordinates of the green LED, respectively.

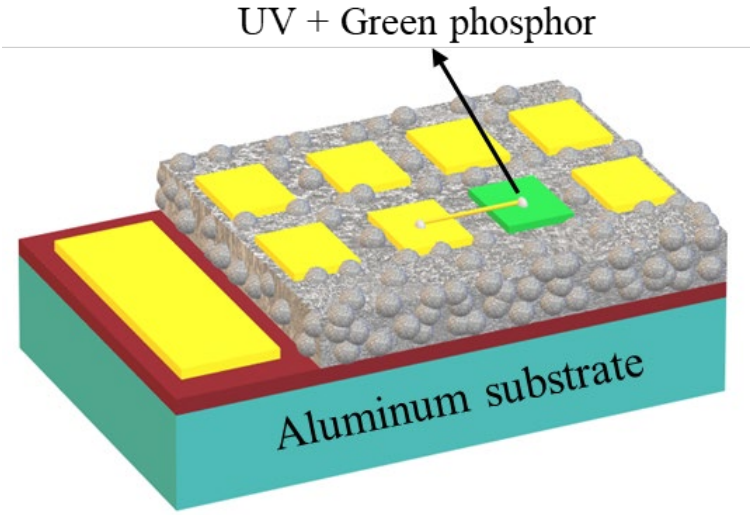

***Figure 36**. Schematic diagram of LEDs connected in parallel with green phosphor on one LED. (Ref 73)*

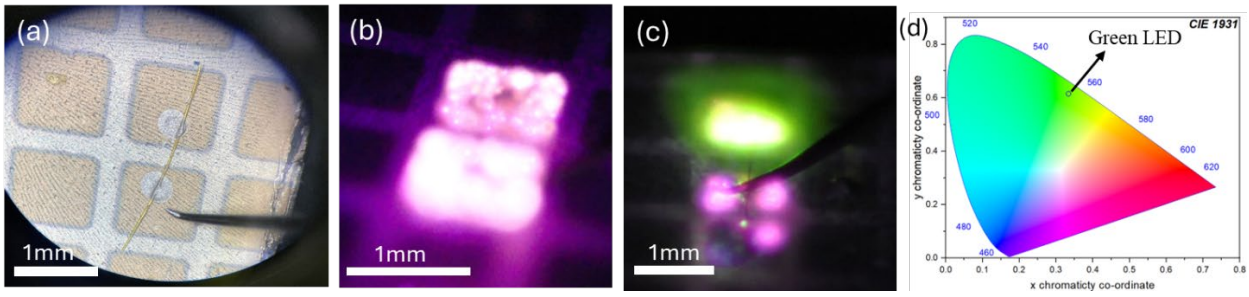

***Figure 37**. **(a)** Photograph of LEDs connected in parallel, **(b)** UV light in parallel, **(c)** green phosphor coated over one LED, **(d)** CIE color space of green LED. (Ref 73)*

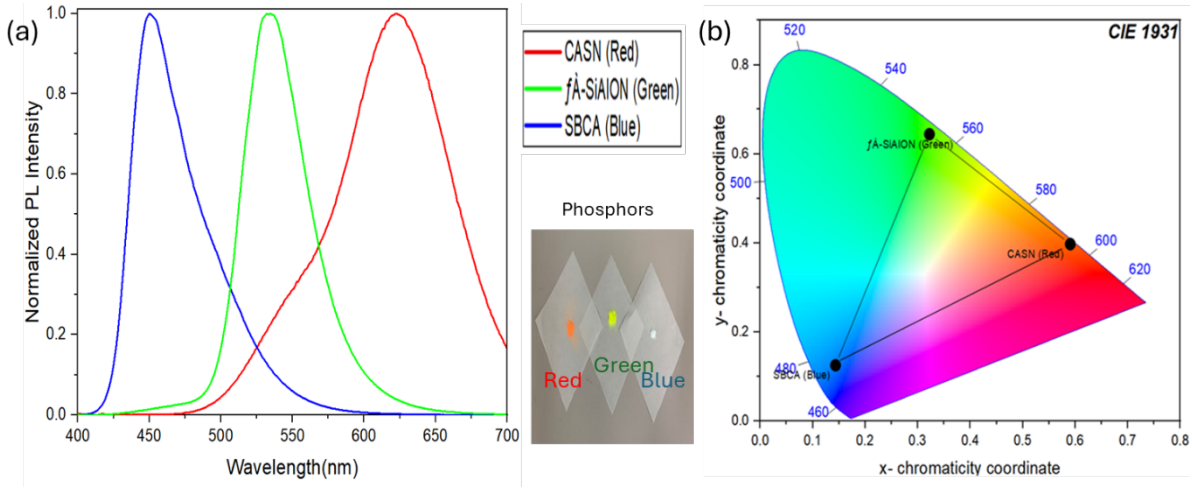

***Figure 38**. **(a)** PL spectra of pc-LEDs, **(b)** color gamut formed by corresponding PL spectra. (Ref 73)*

This setup is comparable to that of a commercial white LED formed by combining a yellow phosphor (Ce:YAG) with a blue chip (InGaN), which is a commonly used material for blue LED excitation. As shown in **Figure 39a**, part of the UV NBE was down-converted into red, green, and blue light, illustrating the EL spectra of the pc-visible LEDs. The color gamut formed by the corresponding visible light is shown in the CIE 1931 color space chromaticity diagram in **Figure 39b**. By choosing phosphors with greater saturation, the gamut area can be further improved. Moreover, the residual UV light emitted by LEDs can be diminished by employing a UV filter or by augmenting the phosphor thickness to optimize the amount of visible light produced.

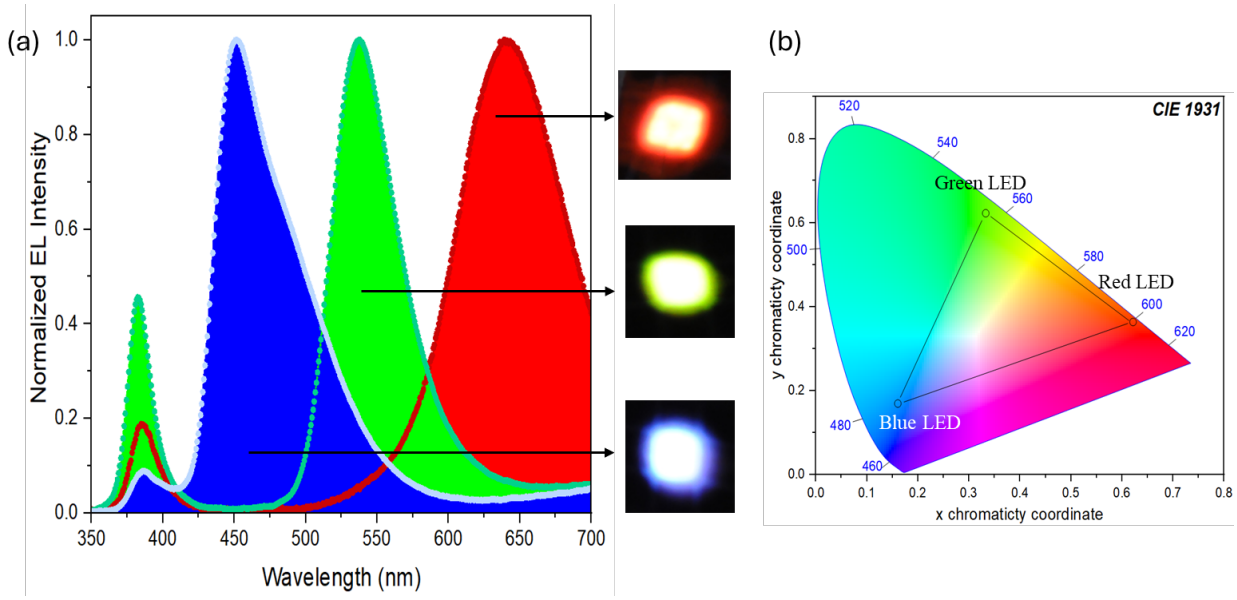

***Figure 39**. **(a)** EL spectra of pc-LEDs, **(b)** schematic diagram of pc-LEDs, **(c)** color gamut formed by corresponding LEDs. (Ref 73)*

5.4.2 White LEDs

To fabricate a WLED, it is essential to down-convert the UV light to visible emission, as shown in **Figure 40a**, which is achieved by using a phosphor blend. The phosphor blend (a mixture of red, green, and blue phosphors) is deposited by a die bonder over a gold electrode, as shown in **Figure 40b**, and is down-converted to emit white light by phosphors, as shown in **Figure 40c**.

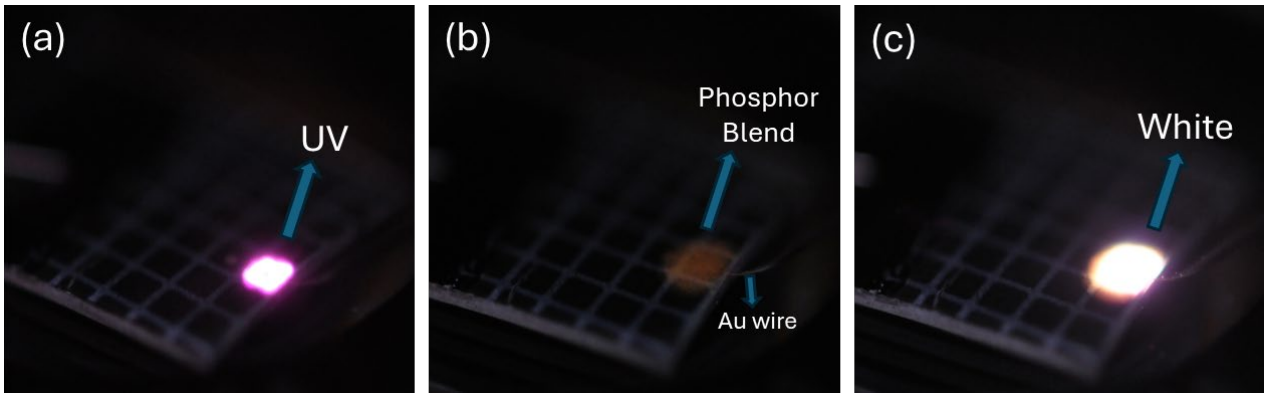

***Figure 40. (a)** UV light before phosphor deposition, **(b)** blend of phosphors deposited, **(c)** white light using multiple phosphors excited by UV light. (Ref 73)*

As shown in **Figure 41 a**, negligible peak shifts for visible regions when compared with UV regions as the injection currents were varied, which eventually led to the high chromatic stability

of the pc-WLED [22]. Furthermore, the chromaticity coordinates of the WLED are plotted in the CIE color space, as shown in **Figure 41b**, which are (0.32, 0.33) in the CIE 1931 color space, very close to the ideal white-light chromaticity coordinate (0.33, 0.33).

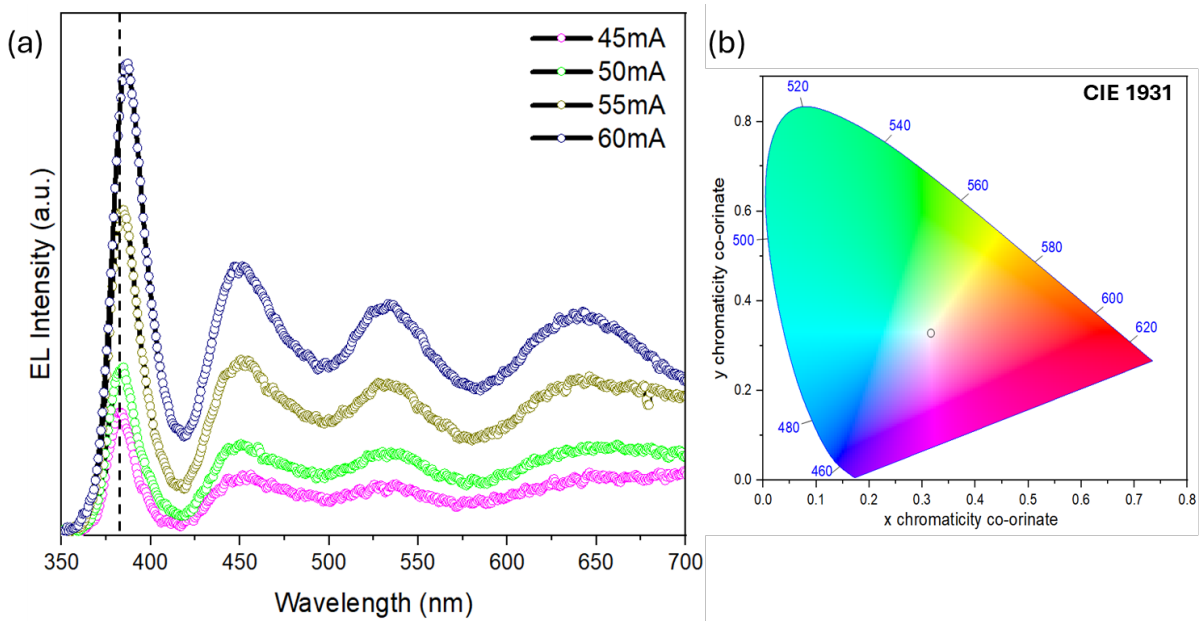

Figure 41. (a) *WLED EL spectra with variable injection current,* ***(b)*** *Spectra of fabricated white LED. (Ref 73)*

5.5 Color rendering index (CRI) and TM-30

Color rendering index means that the extent to which reflected light from a source includes the infinity of colors existing in the spectrum of the reference source, normally daylight or an incandescent lamp. For WLEDs, also applied in a wide range of applications, from general lighting to backlighting, the CRI may be different based on the kind of LED used. CRI values of WLEDs normally range from about 70 to over 90. The more the CRI value, the better for a light source to render colors more accurately and unveil the true color of objects illuminated with this light [2].

The average color rendering index of the fabricated WLED was approximately (CRI, $R_a = 90$), and the correlated color temperature (CCT) was approximately 6226 K, corresponding to cool white

light. It's good to note, though, that even as CRI is an interesting metric to measure color accuracy, it doesn't give the full picture of the quality of light.

TM-30 is the method developed by the Illuminating Engineering Society to evaluate the color rendition properties of light sources; it is aimed at providing more information on how light sources render colors than what was conventionally done with the CRI. As in CRI, the TM-30 comprises an index calculating the Color Fidelity Index, R_f, which states the degree by which a given light source can radically and precisely render colors in comparison with a reference source. Unlike in CRI, TM-30 makes use of a far more comprehensive set of color samples with advanced criteria of evaluation to come up with color fidelity. Another addition it makes is a metric for estimating the average change in chroma for a set of samples called the Color Gamut Index (R_g). R_g gives information about the saturation of colors under the light source and hence is information not captured by traditional color rendering metrics. TM-30 color vector graphics plot hue and saturation shifts that occur when the items are lit using the light source being evaluated, making them easier to understand in terms of what the light source does to most colors. TM-30 offers additional information beyond R_f and R_g by including individual fidelity and gamut values for each color sample, together with information on hue shifts in terms of both direction and magnitude.

The TM-30 20 data for the fabricated WLED is shown in **Figure 42a**, (R_f = 93) and (R_g = 106). Graphical reports that plot the color averages for 16 hue bins for color fidelity and chroma shift are shown in **Figure 42b** and **Figure 42c**, respectively. For most hue bins, the value of color fidelity is more than 85, indicating better color reproduction.

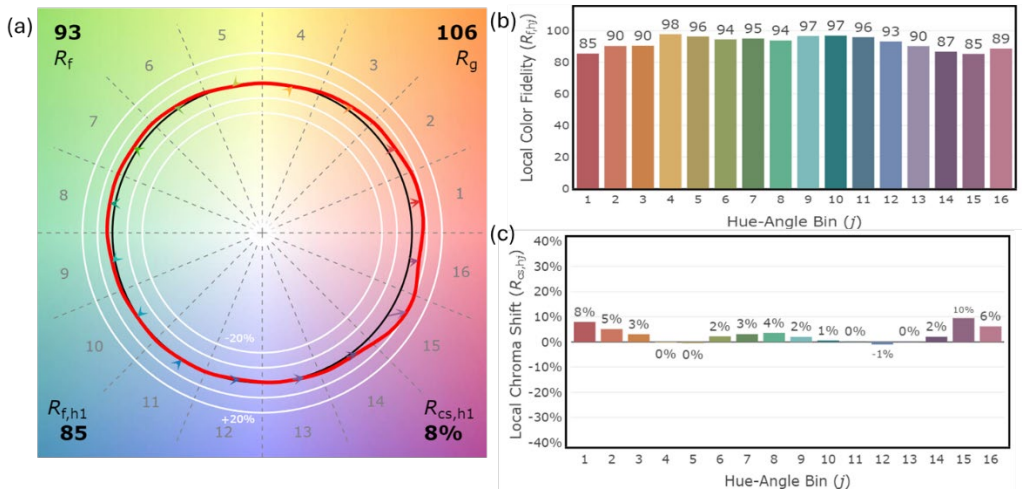

Figure 42. ***(a)*** *TM-30-20 color vector graphics,* ***(b)*** *local chroma fidelity with respect to hue-angle bin,* ***(c)*** *local chroma shifts with respect to hue-angle bin of pc-WLED. (Ref 73)*

5.6 Conclusion

The nanoparticle-based homojunction diode showed near-UV electroluminescence emission both at room temperature and elevated temperatures. However, a reduction in EL was observed as the value of the injection current exceeded the threshold, mainly at high LED surface temperatures. A part of the UV light was absorbed by the phosphors to result in visible emissions in the subsequent step. A multiple-phosphor-based method confirmed the high optical stability combined with color-rendering properties of the white LED.

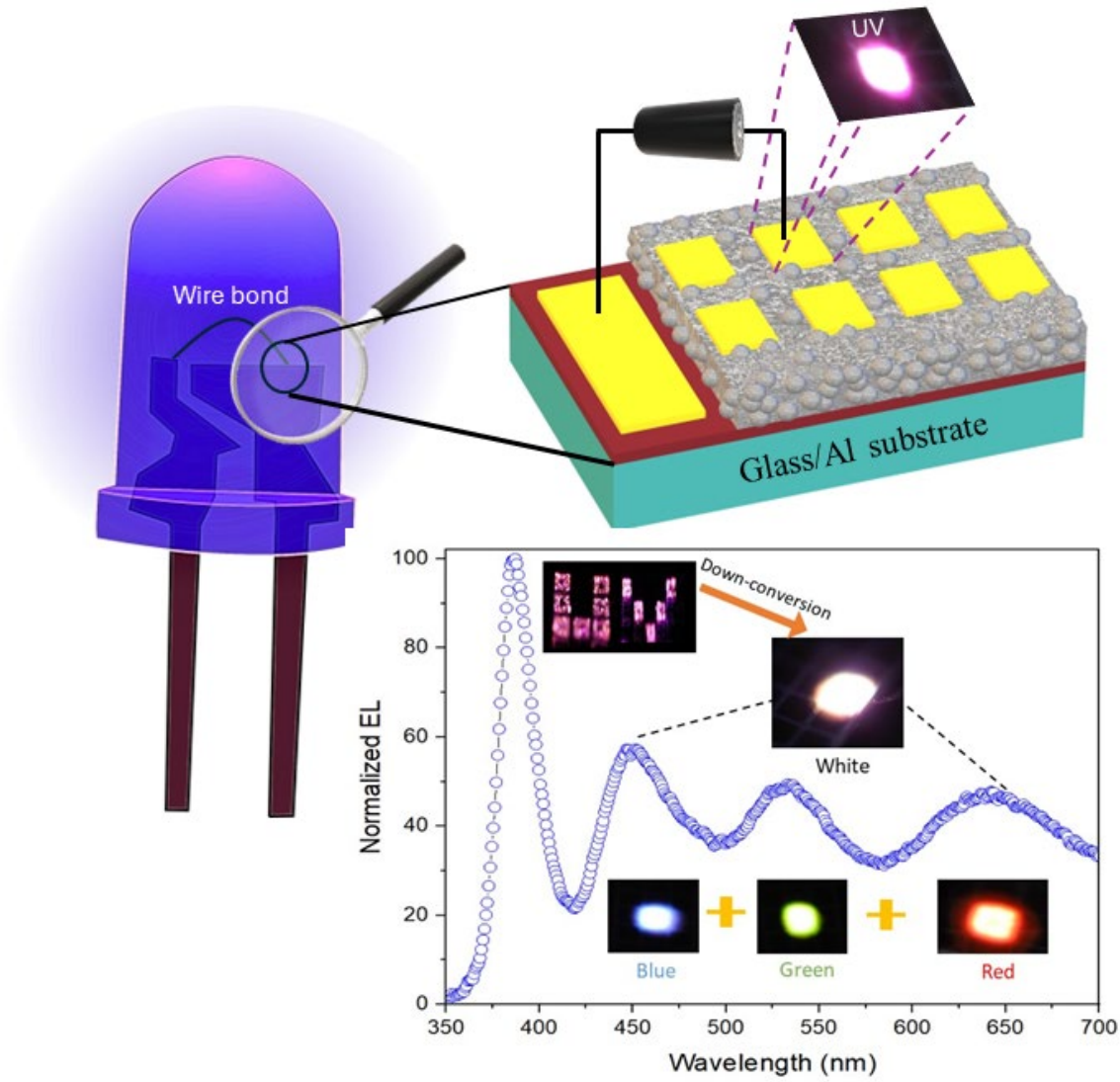

Major research findings of chapter 5 have been published (Deep, R., Yoshida, T., & Fujita, Y. (2024), "Full-Color Electroluminescence from ZnO-Nanoparticles-based Homojunction Diodes". physica status solidi (RRL)–Rapid Research Letters. https://doi.org/10.1002/pssr.202400149).

Chapter 6. Summary and recommendations for future work

The process of nitrogen-doped ZnO nanoparticle fabrication was successfully achieved using DC arc plasma gas evaporation. Additionally, the generation process was evaluated spectroscopically. The addition of nitrogen dopants is advantageous at the low plasma temperature, and they function as acceptors in the ZnO NPs. This is further confirmed by the creation of light-emitting diodes based on these NPs.

Impact of defects in nitrogen-doped ZnO NPs through the experimental fabrication of LEDs utilizing these NPs. The experimental findings demonstrate that defects related to zinc vacancies in nitrogen-doped ZnO function as acceptors and contribute to the improvement of ZnO's p-type characteristics.

Near-UV electroluminescence emission was observed for the nanoparticle-based homojunction diode at both room temperature and elevated temperatures. A proportion of UV light is down-converted into visible light using phosphors. Better color-rendering and high optical stability properties of the white LED were confirmed using a multi-phosphor-based approach.

The color-rendering properties of the white LED can be further improved by adjusting the phosphor ratio or by utilizing more efficient phosphors. The role of defects in ZnO NPs can be further verified by theoretical methods like density functional methods.

References

[1] P. Seidenberg, “From Germanium to Silicon”.

[2] J. Cho, J. H. Park, J. K. Kim, and E. F. Schubert, “White light-emitting diodes: History, progress, and future,” *Laser & Photonics Reviews*, vol. 11, no. 2, p. 1600147, Mar. 2017, doi: 10.1002/lpor.201600147.

[3] F. Rahman, “Zinc oxide light-emitting diodes: a review,” *Opt. Eng.*, vol. 58, no. 01, p. 1, Jan. 2019, doi: 10.1117/1.OE.58.1.010901.

[4] S. Nakamura, T. Mukai, and M. Senoh, “Candela-class high-brightness InGaN/AlGaN double-heterostructure blue-light-emitting diodes,” *Applied Physics Letters*, vol. 64, no. 13, pp. 1687–1689, Mar. 1994, doi: 10.1063/1.111832.

[5] B. Deka Boruah, “Zinc oxide ultraviolet photodetectors: rapid progress from conventional to self-powered photodetectors,” *Nanoscale Adv.*, vol. 1, no. 6, pp. 2059–2085, 2019, doi: 10.1039/C9NA00130A.

[6] A. Tsukazaki *et al.*, “Repeated temperature modulation epitaxy for p-type doping and light-emitting diode based on ZnO,” *Nature Mater*, vol. 4, no. 1, pp. 42–46, Jan. 2005, doi: 10.1038/nmat1284.

[7] S. Chu *et al.*, “Electrically pumped waveguide lasing from ZnO nanowires,” *Nature Nanotech*, vol. 6, no. 8, pp. 506–510, Aug. 2011, doi: 10.1038/nnano.2011.97.

[8] C. Cao, B. Zhang, and S. Lin, “p-type ZnO for photocatalytic water splitting,” *APL Materials*, vol. 10, no. 3, p. 030901, Mar. 2022, doi: 10.1063/5.0083753.

[9] H. Saadi, Z. Benzarti, P. Sanguino, J. Pina, N. Abdelmoula, and J. S. S. de Melo, “Enhancing the electrical conductivity and the dielectric features of ZnO nanoparticles through Co doping effect for energy storage applications,” *J Mater Sci: Mater Electron*, vol. 34, no. 2, p. 116, Jan. 2023, doi: 10.1007/s10854-022-09470-5.

[10] D. R. Miller, S. A. Akbar, and P. A. Morris, “Nanoscale metal oxide-based heterojunctions for gas sensing: A review,” *Sensors and Actuators B: Chemical*, vol. 204, pp. 250–272, Dec. 2014, doi: 10.1016/j.snb.2014.07.074.

[11] K. Senthilkumar *et al.*, “Preparation of ZnO nanoparticles for bio-imaging applications,” *physica status solidi (b)*, vol. 246, no. 4, pp. 885–888, 2009, doi: https://doi.org/10.1002/pssb.200880606.

[12] J. Bao, M. A. Zimmler, F. Capasso, X. Wang, and Z. F. Ren, "Broadband ZnO Single-Nanowire Light-Emitting Diode," *Nano Lett.*, vol. 6, no. 8, pp. 1719–1722, Aug. 2006, doi: 10.1021/nl061080t.

[13] S. Raha and Md. Ahmaruzzaman, "ZnO nanostructured materials and their potential applications: progress, challenges and perspectives," *Nanoscale Adv.*, vol. 4, no. 8, pp. 1868–1925, 2022, doi: 10.1039/D1NA00880C.

[14] J. N. Hasnidawani, H. N. Azlina, H. Norita, N. N. Bonnia, S. Ratim, and E. S. Ali, "Synthesis of ZnO Nanostructures Using Sol-Gel Method," *Procedia Chemistry*, vol. 19, pp. 211–216, 2016, doi: 10.1016/j.proche.2016.03.095.

[15] P. M. Aneesh, K. A. Vanaja, and M. K. Jayaraj, "Synthesis of ZnO nanoparticles by hydrothermal method," presented at the NanoScience + Engineering, Z. Gaburro and S. Cabrini, Eds., San Diego, California, USA, Sep. 2007, p. 66390J. doi: 10.1117/12.730364.

[16] A. V. Avdeeva, X. Zang, A. G. Muradova, and E. V. Yurtov, "Formation of Zinc-Oxide Nanorods by the Precipitation Method," *Semiconductors*, vol. 51, no. 13, pp. 1724–1727, Dec. 2017, doi: 10.1134/S1063782617130036.

[17] S. Hajiashrafi and N. Motakef Kazemi, "Preparation and evaluation of ZnO nanoparticles by thermal decomposition of MOF-5," *Heliyon*, vol. 5, no. 9, p. e02152, Sep. 2019, doi: 10.1016/j.heliyon.2019.e02152.

[18] G. P. Zhu, C. X. Xu, X. F. Wu, Y. Yang, X. W. Sun, and Y. P. Cui, "Zinc Oxide Nanorods Grown by Arc Discharge," *Journal of Elec Materi*, vol. 36, no. 4, pp. 494–497, May 2007, doi: 10.1007/s11664-006-0068-2.

[19] Y. Hiragino *et al.*, "Synthesis of nitrogen-doped ZnO nanoparticles by RF thermal plasma," *Solid-State Electronics*, vol. 118, pp. 41–45, Apr. 2016, doi: 10.1016/j.sse.2016.01.003.

[20] Y. Fujita, K. Moriyama, Y. Hiragino, Y. Furubayashi, H. Hashimoto, and T. Yoshida, "Electroluminescence from nitrogen doped ZnO nanoparticles," *Phys. Status Solidi C*, vol. 11, no. 7–8, pp. 1260–1262, Jul. 2014, doi: 10.1002/pssc.201300645.

[21] I. M. Shafiqul, T. Yoshida, and Y. Fujita, "p-ZnO/n-ZnMgO Nanoparticle-Based Heterojunction UV Light-Emitting Diodes," *Materials*, vol. 15, no. 23, p. 8348, Nov. 2022, doi: 10.3390/ma15238348.

[22] J. K. Sheu *et al.*, "White-light emission from near UV InGaN-GaN LED chip precoated with blue/green/red phosphors," *IEEE Photon. Technol. Lett.*, vol. 15, no. 1, pp. 18–20, Jan. 2003, doi: 10.1109/LPT.2002.805852.

[23] P. M. Lewis, D. Hebbar N., K. S. Choudhari, and S. D. Kulkarni, "White light-emitting ZnO nanoparticles exhibiting color temperature tunability with near UV excitation and high color rendering," *Materials Science in Semiconductor Processing*, vol. 138, p. 106284, Feb. 2022, doi: 10.1016/j.mssp.2021.106284.

[24] Ü. Özgür *et al.*, "A comprehensive review of ZnO materials and devices," *Journal of Applied Physics*, vol. 98, no. 4, p. 041301, Aug. 2005, doi: 10.1063/1.1992666.

[25] Y.-S. Choi, J.-W. Kang, D.-K. Hwang, and S.-J. Park, "Recent Advances in ZnO-Based Light-Emitting Diodes," *IEEE Trans. Electron Devices*, vol. 57, no. 1, pp. 26–41, Jan. 2010, doi: 10.1109/TED.2009.2033769.

[26] M.-S. Oh, D.-K. Hwang, J.-H. Lim, Y.-S. Choi, and S.-J. Park, "Current-driven hydrogen incorporation in zinc oxide," *Applied Physics Letters*, vol. 91, no. 21, p. 212102, Nov. 2007, doi: 10.1063/1.2816119.

[27] C. G. Van De Walle, "Hydrogen as a Cause of Doping in Zinc Oxide," *Phys. Rev. Lett.*, vol. 85, no. 5, pp. 1012–1015, Jul. 2000, doi: 10.1103/PhysRevLett.85.1012.

[28] D. C. Look, J. W. Hemsky, and J. R. Sizelove, "Residual Native Shallow Donor in ZnO," *Phys. Rev. Lett.*, vol. 82, no. 12, pp. 2552–2555, Mar. 1999, doi: 10.1103/PhysRevLett.82.2552.

[29] K. Bandopadhyay and J. Mitra, "Zn interstitials and O vacancies responsible for n-type ZnO: what do the emission spectra reveal?," *RSC Adv.*, vol. 5, no. 30, pp. 23540–23547, 2015, doi: 10.1039/C5RA00355E.

[30] N. Ito, Y. Sato, P. K. Song, A. Kaijio, K. Inoue, and Y. Shigesato, "Electrical and optical properties of amorphous indium zinc oxide films," *Thin Solid Films*, vol. 496, no. 1, pp. 99–103, Feb. 2006, doi: 10.1016/j.tsf.2005.08.257.

[31] M.-S. Oh, D.-K. Hwang, D.-J. Seong, H.-S. Hwang, S.-J. Park, and E. Do Kim, "Improvement of Characteristics of Ga-Doped ZnO Grown by Pulsed Laser Deposition Using Plasma-Enhanced Oxygen Radicals," *J. Electrochem. Soc.*, vol. 155, no. 9, p. D599, 2008, doi: 10.1149/1.2952077.

[32] K.-K. Kim *et al.*, "High electron concentration and mobility in Al-doped n-ZnO epilayer achieved via dopant activation using rapid-thermal annealing," *Journal of Applied Physics*, vol. 97, no. 6, p. 066103, Mar. 2005, doi: 10.1063/1.1863416.

[33] E. Chikoidze, M. Modreanu, V. Sallet, O. Gorochov, and P. Galtier, "Electrical properties of chlorine-doped ZnO thin films grown by MOCVD," *Physica Status Solidi (a)*, vol. 205, no. 7, pp. 1575–1579, Jul. 2008, doi: 10.1002/pssa.200723192.

[34] R. Yang *et al.*, "ZnO with p-Type Doping: Recent Approaches and Applications," *ACS Appl. Electron. Mater.*, vol. 5, no. 8, pp. 4014–4034, Aug. 2023, doi: 10.1021/acsaelm.3c00515.

[35] A. Valentini, F. Quaranta, M. Rossi, and G. Battaglin, "Preparation and characterization of Li-doped ZnO films," *Journal of Vacuum Science & Technology A: Vacuum, Surfaces, and Films*, vol. 9, no. 2, pp. 286–289, Mar. 1991, doi: 10.1116/1.577502.

[36] L. L. Yang, Z. Z. Ye, L. P. Zhu, Y. J. Zeng, Y. F. Lu, and B. H. Zhao, "Fabrication of p-Type ZnO Thin Films via DC Reactive Magnetron Sputtering by Using Na as the Dopant Source," *Journal of Elec Materi*, vol. 36, no. 4, pp. 498–501, May 2007, doi: 10.1007/s11664-006-0047-7.

[37] Y. K. Yasuo Kanai, "Admittance Spectroscopy of Cu-Doped ZnO Crystals," *Jpn. J. Appl. Phys.*, vol. 30, no. 4R, p. 703, Apr. 1991, doi: 10.1143/JJAP.30.703.

[38] Y. K. Yasuo Kanai, "Admittance Spectroscopy of ZnO Crystals Containing Ag," *Jpn. J. Appl. Phys.*, vol. 30, no. 9R, p. 2021, Sep. 1991, doi: 10.1143/JJAP.30.2021.

[39] T. Aoki, Y. Shimizu, A. Miyake, A. Nakamura, Y. Nakanishi, and Y. Hatanaka, "p-Type ZnO Layer Formation by Excimer Laser Doping," *phys. stat. sol. (b)*, vol. 229, no. 2, pp. 911–914, Jan. 2002, doi: 10.1002/1521-3951(200201)229:2<911::AID-PSSB911>3.0.CO;2-R.

[40] S. P. Wang *et al.*, "A facile route to arsenic-doped p-type ZnO films," *Journal of Crystal Growth*, vol. 311, no. 14, pp. 3577–3580, Jul. 2009, doi: 10.1016/j.jcrysgro.2009.06.002.

[41] X. H. Pan *et al.*, "Electrical and optical properties of phosphorus-doped p-type ZnO films grown by metalorganic chemical vapor deposition," *Journal of Applied Physics*, vol. 103, no. 2, p. 023708, Jan. 2008, doi: 10.1063/1.2828017.

[42] D. C. Look, D. C. Reynolds, C. W. Litton, R. L. Jones, D. B. Eason, and G. Cantwell, "Characterization of homoepitaxial *p* -type ZnO grown by molecular beam epitaxy," *Applied Physics Letters*, vol. 81, no. 10, pp. 1830–1832, Sep. 2002, doi: 10.1063/1.1504875.

[43] Y. J. Zeng *et al.*, "Study on the Hall-effect and photoluminescence of N-doped p-type ZnO thin films," *Materials Letters*, vol. 61, no. 1, pp. 41–44, Jan. 2007, doi: 10.1016/j.matlet.2006.04.001.

[44] T. Yamamoto, "Codoping for the fabrication of p-type ZnO," *Thin Solid Films*, vol. 420–421, pp. 100–106, Dec. 2002, doi: 10.1016/S0040-6090(02)00655-7.

[45] M.-J. Chen, J.-R. Yang, and M. Shiojiri, "ZnO-based ultra-violet light emitting diodes and nanostructures fabricated by atomic layer deposition," *Semicond. Sci. Technol.*, vol. 27, no. 7, p. 074005, Jul. 2012, doi: 10.1088/0268-1242/27/7/074005.

[46] C. Yuen, S. F. Yu, S. P. Lau, Rusli, and T. P. Chen, "Fabrication of n-ZnO:Al/p-SiC(4H) heterojunction light-emitting diodes by filtered cathodic vacuum arc technique," *Appl. Phys. Lett.*, vol. 86, no. 24, p. 241111, Jun. 2005, doi: 10.1063/1.1947889.

[47] A. Baltakesmez, S. Tekmen, P. Köç, S. Tüzemen, K. Meral, and Y. Onganer, "UV-visible detector and LED based n-ZnO/p-Si heterojunction formed by electrodeposition," *AIP Advances*, vol. 3, no. 3, p. 032125, Mar. 2013, doi: 10.1063/1.4795737.

[48] F. Zhuge *et al.*, "ZnO p-n homojunctions and ohmic contacts to Al–N-co-doped p-type ZnO," *Applied Physics Letters*, vol. 87, no. 9, p. 092103, Aug. 2005, doi: 10.1063/1.2012521.

[49] A. Tsukazaki *et al.*, "Blue Light-Emitting Diode Based on ZnO," *Jpn. J. Appl. Phys.*, vol. 44, no. 5L, p. L643, May 2005, doi: 10.1143/JJAP.44.L643.

[50] A. Chen *et al.*, "Beryllium-Assisted p-Type Doping for ZnO Homojunction Light-Emitting Devices," *Adv. Funct. Mater.*, vol. 26, no. 21, pp. 3696–3702, Jun. 2016, doi: 10.1002/adfm.201600163.

[51] N. X. Sang, T. C. Beng, T. Jie, E. A. Fitzgerald, and C. S. Jin, "Fabrication of p-type ZnO nanorods/n-GaN film heterojunction ultraviolet light-emitting diodes by aqueous solution method: Fabrication of ZnO nanorods/n-GaN film heterojunction LEDs," *Phys. Status Solidi A*, vol. 210, no. 8, pp. 1618–1623, Aug. 2013, doi: 10.1002/pssa.201228643.

[52] E. F. SCHUBERT, *LIGHT-EMITTING DIODES*. E FRED SCHUBERT, 2018.

[53] N. Kamarulzaman, M. F. Kasim, and N. F. Chayed, "Elucidation of the highest valence band and lowest conduction band shifts using XPS for ZnO and Zn 0.99 Cu 0.01 O band gap changes," *Results in Physics*, vol. 6, pp. 217–230, 2016, doi: 10.1016/j.rinp.2016.04.001.

[54] K. J. Saji, N. V. Joshy, and M. K. Jayaraj, "Optical emission spectroscopic studies on laser ablated zinc oxide plasma," *Journal of Applied Physics*, vol. 100, no. 4, p. 043302, Aug. 2006, doi: 10.1063/1.2266260.

[55] R. Deep, T. Akazawa, T. Yoshida, and Y. Fujita, “A Spectroscopic Evaluation of the Generation Process of Semiconductor Nanoparticles (ZnO) by DC Arc Plasma,” *J*, vol. 6, no. 2, pp. 207–219, Apr. 2023, doi: 10.3390/j6020016.

[56] H. Kato, T. Yamamuro, A. Ogawa, and M. Sano, “Impact of Mixture Gas Plasma of N$_{2}$ and O$_{2}$ as the N Source on ZnO-Based Ultraviolet Light-Emitting Diodes Fabricated by Molecular Beam Epitaxy,” *Appl. Phys. Express*, vol. 4, no. 9, p. 091105, Aug. 2011, doi: 10.1143/APEX.4.091105.

[57] K. Senthilkumar, O. Senthilkumar, S. Morito, T. Ohba, and Y. Fujita, “Synthesis of zinc oxide nanoparticles by dc arc dusty plasma,” *J Nanopart Res*, vol. 14, no. 10, p. 1205, Oct. 2012, doi: 10.1007/s11051-012-1205-x.

[58] M. Hanif, M. Salik, and M. A. Baig, “Laser Based Optical Emission Studies of Zinc Oxide (ZnO) Plasma,” *Plasma Chem Plasma Process*, vol. 33, no. 6, pp. 1167–1178, Dec. 2013, doi: 10.1007/s11090-013-9478-0.

[59] A. Zeuner *et al.*, “Nitrogen doping in bulk and epitaxial ZnO,” *phys. stat. sol. (c)*, vol. 1, no. 4, pp. 731–734, Mar. 2004, doi: 10.1002/pssc.200304255.

[60] H. Mahdhi, J. L. Gauffier, K. Djessas, and Z. B. Ayadi, “Thickness dependence of properties Ga-doped ZnO thin films deposited by magnetron sputtering,” *J Mater Sci: Mater Electron*, vol. 28, no. 6, pp. 5021–5028, Mar. 2017, doi: 10.1007/s10854-016-6158-x.

[61] B. Khalfallah, F. Chaabouni, G. Schmerber, A. Dinia, and M. Abaab, “Investigation of physico-chemical properties of conductive Ga-doped ZnO thin films deposited on glass and silicon wafers by RF magnetron sputtering,” *J Mater Sci: Mater Electron*, vol. 28, no. 1, pp. 75–85, Jan. 2017, doi: 10.1007/s10854-016-5494-1.

[62] I. M. Shafiqul, R. Deep, J. Lin, T. Yoshida, and Y. Fujita, “Demonstration and Evaluation of p-Type and n-Type ZnO Nanoparticles-Based Homojunction UV Light-Emitting Diodes,” *Physica Rapid Research Ltrs*, vol. 16, no. 5, p. 2100556, May 2022, doi: 10.1002/pssr.202100556.

[63] D. Itohara, K. Shinohara, T. Yoshida, and Y. Fujita, “p-Channel and n-Channel Thin-Film-Transistor Operation on Sprayed ZnO Nanoparticle Layers,” *Journal of Nanomaterials*, vol. 2016, pp. 1–6, 2016, doi: 10.1155/2016/8219326.

[64] L. Guo, Y. L. Ji, H. Xu, P. Simon, and Z. Wu, “Regularly Shaped, Single-Crystalline ZnO Nanorods with Wurtzite Structure,” *J. Am. Chem. Soc.*, vol. 124, no. 50, pp. 14864–14865, Dec. 2002, doi: 10.1021/ja027947g.

[65] C.-C. Yang, C.-C. Lin, C.-H. Peng, and S.-Y. Chen, "Effect of annealing atmosphere on physical characteristics and photoluminescence properties of nitrogen-implanted ZnO thin films," *Journal of Crystal Growth*, vol. 285, no. 1–2, pp. 96–102, Nov. 2005, doi: 10.1016/j.jcrysgro.2005.07.048.

[66] K. Senthilkumar, M. Tokunaga, H. Okamoto, O. Senthilkumar, and Y. Fujita, "Hydrogen related defect complexes in ZnO nanoparticles," *Applied Physics Letters*, vol. 97, no. 9, p. 091907, Aug. 2010, doi: 10.1063/1.3485049.

[67] R. Deep, T. Yoshida, and Y. Fujita, "Defects in Nitrogen-Doped ZnO Nanoparticles and Their Effect on Light-Emitting Diodes," *Nanomaterials*, vol. 14, no. 11, p. 977, Jun. 2024, doi: 10.3390/nano14110977.

[68] S. Mishra *et al.*, "Cathodoluminescent Imaging of ZnO:N Films: Study of Annealing Processes Leading to Enhanced Acceptor Luminescence," *Physica Status Solidi (a)*, vol. 220, no. 10, p. 2200466, May 2023, doi: 10.1002/pssa.202200466.

[69] A. Kaschner *et al.*, "Nitrogen-related local vibrational modes in ZnO:N," *Applied Physics Letters*, vol. 80, no. 11, pp. 1909–1911, Mar. 2002, doi: 10.1063/1.1461903.

[70] M. M. Islam, T. Yoshida, and Y. Fujita, "Effects of Ambience on Thermal-Diffusion Type Ga-doping Process for ZnO Nanoparticles," *Coatings*, vol. 12, no. 1, p. 57, Jan. 2022, doi: 10.3390/coatings12010057.

[71] B. Chavillon *et al.*, "P-Type Nitrogen-Doped ZnO Nanoparticles Stable under Ambient Conditions," *J. Am. Chem. Soc.*, vol. 134, no. 1, pp. 464–470, Jan. 2012, doi: 10.1021/ja208044k.

[72] G. B. Nair, H. C. Swart, and S. J. Dhoble, "A review on the advancements in phosphor-converted light emitting diodes (pc-LEDs): Phosphor synthesis, device fabrication and characterization," *Progress in Materials Science*, vol. 109, p. 100622, Apr. 2020, doi: 10.1016/j.pmatsci.2019.100622.

[73] R. Deep, T. Yoshida, and Y. Fujita, "Full-Color Electroluminescence from ZnO-Nanoparticles-based Homojunction Diodes," *physica status solidi (RRL)–Rapid Research Letters*.

List of publications

Journal Papers

Related Publications:

1. **Deep, R.**, Yoshida, T., & Fujita, Y. (2024), "*Full-Color Electroluminescence from ZnO-Nanoparticles-based Homojunction Diodes*". physica status solidi (RRL)–Rapid Research Letters. https://doi.org/10.1002/pssr.202400149.
2. **Deep, R.**, Yoshida, T., & Fujita, Y. (2024), "*Defects in Nitrogen-Doped ZnO Nanoparticles and Their Effect on Light-Emitting Diodes*". Nanomaterials, 14(11), 977.
3. **Deep, R.**, Akazawa, T., Yoshida, T., & Fujita, Y. (2023), "*A Spectroscopic Evaluation of the Generation Process of Semiconductor Nanoparticles (ZnO) by DC Arc Plasma*", J, 6(2), 207-219.

Reference Publications:

4. Shafiqul, I. M., **Deep, R.**, Yoshida, T., Lin, J. & Fujita, Y. (2022), "*Demonstration and Evaluation of p-Type and n-Type ZnO Nanoparticles-Based Homojunction UV Light-Emitting Diodes*". Physica status solidi (RRL)–Rapid Research Letters. 16(5), 2100556.
5. Shafiqul, I. M., **Deep, R.**, Yoshida, T., Lin, J. & Fujita, Y. (2022), "*The role of nitrogen dopants in ZnO nanoparticle-based light emitting diodes*". Nanomaterials, 12(3), 358.

Conference Papers and Presentations

Conference Paper:

1. **Raj Deep**, Takuma Akazawa, Toshiyuki Yoshida, Yasuhisa Fujita, "*Phosphor-Converted white light emitting diodes based on ZnO Nanoparticles*", The 59th Japan Electronic Materials Technology Association 2022, Vol. 54, Bulletin of Japan Electronic Materials Society.

Conference Presentations:

2. **Raj Deep**, "*Solution-processed ZnO Nanoparticles based light emitting diodes*", 15th Hope Meeting with Nobel Laureates 2024, Poster presentation, JP13. (**JSPS HOPE Fellow**)
3. **Raj Deep**, Toshiyuki Yoshida, Yasuhisa Fujita, "*Influence of annealing atmosphere on ZnO nanoparticles based LEDs*", MRM2023/IUMRS-ICA2023 Grand Meeting, Poster presentation (abstract- D1-P304-07). (**Poster award**)
4. **Raj Deep**, Takuma Akazawa, Toshiyuki Yoshida, Yasuhisa Fujita, "*Mechanism of Nitrogen Doping of Zinc Oxide Nanoparticles by Arc Plasma and Study of Their p-type Characteristics*". The 70th JSAP Spring Meeting 2023, Oral presentation (abstract- 15a-E102-10).
5. **Raj Deep**, Takuma Akazawa, Toshiyuki Yoshida and Yasuhisa Fujita, "*Phosphor-converted white light emitting diodes based on ZnO nanoparticle*". The 59th Japan Electronic Materials Technology Association 2022, Oral presentation. (**Encouragement award**)

6. **Raj Deep**, Akazawa Takuma, Toshiyuki Yoshida, Yasuhisa Fujita, "*White light emitting diodes based on ZnO nanoparticles using phosphors*". The JSAP 83rd Autumn Meeting 2022, Poster presentation (abstract- 23a-P06-20). (**Poster award**)
7. **Raj Deep**, Islam Mohammad Shafiqul, Akazawa Takuma, Toshiyuki Yoshida, Yasuhisa Fujita, "*Peak shift and Temperature effects in ZnO nanoparticles-based solution-processed LEDs*". The JSAP 69th Spring Meeting 2022, Oral presentation (abstract- 25a-E202-4).
8. **Raj Deep**, Yuki Konishi, Islam Mohammad Shafiqul, Jie Lin, Toshiyuki Yoshida, Yasuhisa Fujita, "*Leakage current reduction in ZnO nanoparticle based near UV-LEDs*", The JSAP 81st Autumn Meeting 2020, Oral presentation (abstract- 9a-Z20-11).
9. **Raj Deep**, Atsuya Tabuchi, Yuki Konishi, Islam Mohammad Shafiqul, Jie Lin, Toshiyuki Yoshida, Yasuhisa Fujita, "*Enhancing power of ZnO nanoparticle LEDs using silica coated silver Nano-particles*", The JSAP 67th Spring Meeting 2020 (abstract- 15a-PA5-1).
10. Akazawa Takuma, **Raj Deep**, Toshiyuki Yoshida, Yasuhisa Fujita, "*The role of nitrogen dopants in ZnO nanoparticle based LED*", The JSAP 83rd Autumn Meeting 2022, Poster presentation (abstract- 23a-P06-21).
11. Islam Mohammad Shafiqul, Yuki Konishi, **Raj Deep**, Jie Lin, Toshiyuki Yoshida, Yasuhisa Fujita, "*The Emission Power of ZnO Nanoparticle-based LEDs enhanced by adding Silica nanoparticles*", The JSAP 68th Spring Meeting 2021, Oral presentation (abstract- 18p-Z33-3).
12. Islam Mohammad Shafiqul, Yuki Konishi, **Raj Deep**, Jie Lin, Toshiyuki Yoshida, Yasuhisa Fujita, "*The Electroluminescence of ZnO nanoparticle-based LEDs improved by inserting a ZnMgO nanoparticles layer*", The JSAP 68th Spring Meeting 2021, Oral presentation (abstract- 18p-Z33-4).

Acknowledgements

First of all, I would like to express my gratitude to Prof. Dr. Yasuhisa Fujita and Dr. Toshiyuki Yoshida for their unwavering support and guidance. I would like to convey my genuine gratitude for their supervision and the learning opportunities provided by them throughout the whole project. I express profound gratitude to both past and current members of the Fujita-Yoshida group for their collaboration and invaluable contributions to the experiments.

I would like to thank Dr. Shafiqul and Dr. Maruful, who guided me in my initial phase by teaching the experimental methodology. I express my gratitude to Mr. Takuma Akazawa for his invaluable aid and support in conducting my experiments. I express my gratitude to the Centre for Integrated Research in Science at Shimane University for their cooperation in providing XRD and FESEM analysis.

I express my gratitude to my parents and friends for their invaluable moral support and unwavering motivation.

I am immensely thankful to the Ministry of Culture, Sports, Science, and Technology (MEXT) of Japan for granting me a scholarship to pursue my studies. I would like to express my gratitude for the assistance received from the MEXT of Japan City Area Program of Shinji Lake and Nakaumi (2009–2012), JSPS KAKENHI Grant Number 25630150, The Canon Foundation, and SNCC (S-Nanotech Co-Creation Co., Ltd.). I would also like to thank all SNCC employees for their insights and collaboration.

Last but not least, I would like to express my gratitude to all my fellow lab mates for their substantial assistance both in terms of academics and social interactions.